# Vertical cloud structure observed from shipborne radar and lidar: Midlatitude case study during the MR01/K02 cruise of the research vessel Mirai

Hajime Okamoto,[1] Tomoaki Nishizawa,[2] Toshihiko Takemura,[3] Hiroshi Kumagai,[4] Hiroshi Kuroiwa,[4] Nobuo Sugimoto,[5] Ichiro Matsui,[5] Atsushi Shimizu,[5] Seita Emori,[5] Akihide Kamei,[6] and Teruyuki Nakajima[7]

Received 7 June 2006; revised 1 December 2006; accepted 11 January 2007; published 28 April 2007.

[1] We observed the vertical distribution of clouds over the Pacific Ocean near Japan in May 2001 using lidar and a 95-GHz radar on the Research Vessel Mirai. Cloud analyses derived from synergy use of radar and lidar observations showed that there were two local maxima of cirrus cloud frequency of occurrence at 7 and 10.5 km and the drizzle frequency of occurrence was about the half compared with that of clouds below 4 km. The number of layers could be also measured using these schemes. Single, double, triple, and quadruple (or more) cloud layers had a 48, 23, 7, and 2% probability of occurrence, respectively. The average number of cloud layers when clouds existed was 1.54. The vertical structure of clouds observed with the radar/lidar system was compared to clouds in the aerosol transport model SPRINTARS, which is based on the CCSR-NIES Atmospheric General Circulation Model. The cloud fraction, radar reflectivity factor, and lidar backscattering coefficient were simulated by the model and compared to those by the observations using height-time cross-sections where the radar sensitivity was taken into account. The overall pattern of cloud fraction was well reproduced, although the model underestimated (overestimated) mean cloud fraction below 8 km (above 8 km). Cloud microphysics in the model could also be validated through comparison of derived model radar and lidar signals in grid mean with observations. The model overestimated ice particle size above 10 km, and simulated particle sizes in water clouds of 10 $\mu$m were larger than observed.

**Citation:** Okamoto, H., et al. (2007), Vertical cloud structure observed from shipborne radar and lidar: Midlatitude case study during the MR01/K02 cruise of the research vessel Mirai, *J. Geophys. Res.*, *112*, D08216, doi:10.1029/2006JD007628.

## 1. Introduction

[2] Radiative impacts of and water cycles in clouds profoundly influence the climate system. Sensors on satellites can record the global distribution of cloud physical properties such as cloud cover, optical thickness, and effective radius [e.g., *Rossow and Schiffer*, 1999]. Despite considerable effort using such satellite-borne sensors, however, uncertainties remain in the assessment of climate impacts due to clouds. The accuracy of satellite measurements is reduced by the presence of multilayered structure and by vertical nonhomogeneity in cloud microphysics. Although the ISCCP data set provides information about the vertical structure of cloud top pressures, it only sees the upper most cloud top. Therefore an overlap assumption is introduced in reproducing the vertical structure of clouds [*Rossow et al.*, 2005]. Related to this nature of the satellites, assumption of a single homogeneous cloud layer is often made in the satellite remote sensing and retrieved properties can include errors in clouds that have many layers. Only quite recently, multilayer structure of clouds is taken into account in the retrieval of cloud microphysics in the analyses of the satellite data [*Chang and Li*, 2005].

[3] In order to overcome the situation, active instruments such as cloud radar and lidar are expected to provide detailed vertical profiles of macroscale and microphysical properties. *Mace et al.* [1997] used 900 hours of cloud radar observations over Pennsylvania to determine cloud macroscale properties in a study that included vertical distributions of clouds, temperature, and synoptic-scale ascent. *Clothiaux et al.* [2000] developed an algorithm to determine

[1]Center for Atmospheric and Oceanic Studies, Graduate School of Science, Tohoku University, Sendai, Japan.
[2]Meteorological Research Institute, Tsukuba, Ibaraki, Japan.
[3]Research Institute for Applied Mechanics, Kyushu University, Kasuga, Fukuoka, Japan.
[4]National Institute of Information and Communications Technology, Koganei, Tokyo, Japan.
[5]National Institute for Environmental Studies, Tsukuba, Ibaraki, Japan.
[6]National Institute of Advanced Industrial Science and Technology, Tsukuba, Japan.
[7]Center for Climate System Research, The University of Tokyo, Kashiwa, Chiba, Japan.


0148-0227/07/2006JD007628$09.00

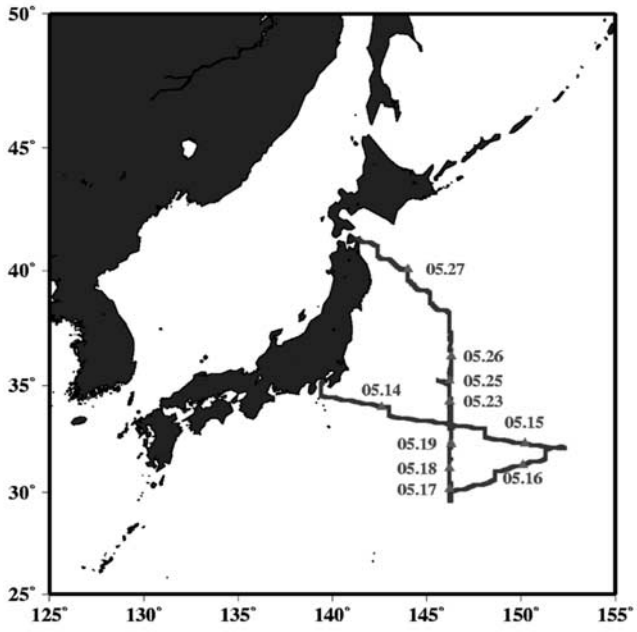


**Figure 1.** Track of cruise MR01/K02 of the research vessel Mirai.

cloud heights using data from a 35-GHz radar, a micropulse lidar, and a Vaisala laser ceilometer, sensors used in the US Department of Energy Atmospheric Radiation Measurement (ARM) program. The radar and the lidar were colocated at cloud and radiation test bed (CART) sites in the southern Great Plains (SGP) of Oklahoma, the North Slope of Alaska (NSA), and in the tropical western Pacific (TWP) on the islands of Nauru and Manus near the equator. *Mace et al.* [2001] used 1 year of 35-GHz radar data collected at the ARM SGP site in Oklahoma to determine macroscale and microphysical properties of midlatitude cirrus clouds. There are very few observations by cloud radar and lidar over oceans. Exceptions are the space-borne lidar observation from the Lidar Inspace Technology Experiment (LITE) [*Hogan et al.*, 2004] or shipborne cloud radar on board *Ron Brown* [*Matrosov et al.*, 2004].

[4] For the validation studies of global climate models, *Mace et al.* [1998a] compared cloud frequency measured with the ground-based 35-GHz cloud radar at the SGP site in Oklahoma in winter with ECMWF model output to validate the model. *Hogan et al.* [2001] compared the vertical distribution of mean cloud fraction observed with 95-GHz radar data in Chilbolton in winter with results from the ECMWF model. However, study of vertical representation of clouds in climate models over oceans has not been sufficient, due also to the lack of the observations in the area. *Wang et al.* [2000] illustrates the differences in cloud vertical properties between land and ocean from the analysis of a 20-year global radio-sonde data set. Clouds over the ocean show more frequent occurrence of multilayer structure than over the land. It is therefore vital to collect the observational data sets of clouds by active sensors over ocean. It is also noted that the comparisons of both the radar and lidar signals between observation and models have not yet been studied.

[5] Our main aims in the paper are to examine the vertical structure of clouds over oceans in midlatitude on the basis of synergy use of ship-born radar and lidar measurements and, at the first time, use these two signals to validate the representation of cloud macroscale and microphysical properties in the climate model.

[6] In this study, we used shipborne radar and lidar data from over the Pacific Ocean near Japan. The radar and lidar were installed on the Research Vessel Mirai, which is operated by the Japan Marine Science and Technology Center (JAMSTEC). The MR01/K02 cruise, conducted in May 2001, was the first cruise with both cloud radar and lidar on board. *Sugimoto et al.* [2002] described the lidar data from the MR01/K02 cruise and presented observations of dust and sulfate. Here we used the same lidar data as presented by *Sugimoto et al.* [2002]. The cloud radar on this cruise was the SPIDER (Super Polarimetric Ice Crystal Detection and Explication Radar), which has also been used for ground-based observations in Kashima, Japan [*Okamoto et al.*, 2003]. Shipborne experiments subsequent to MR01/K02 also recorded cloud radar and lidar data, including a cruise in the tropics from September to December 2001. Comprehensive analyses of these data will be presented in another paper.

[7] Section 2 details the radar and lidar data used in this study. Five different cloud mask schemes to determine cloud occurrence from radar and lidar data are explained in section 3. Section 4 examines the height-time cross-section of cloud occurrence as derived from each cloud mask scheme. Together with clouds, we examined drizzle frequency of occurrence. Properties of the multilayer cloud structure are also discussed. Section 5 compares cloud radar and lidar signals (i.e., actual observations) to simulated signals derived from the output of SPRINTARS, an aerosol transport model that explicitly models clouds and aerosols and is based on the CCSR-NIES General Circulation Models (CCSR-NIES GCM; *Takemura et al.* [2000, 2005]). Comparisons of radar and lidar signals help validate model performance not only for cloud macroscale properties but also for cloud and aerosol microphysics. Section 6 summarizes the findings.

## 2. Observational Data Set of the 95-GHZ Radar and the Lidar

[8] Two shipborne experiments involved the use of a 95-GHz cloud radar and a lidar onboard the Research Vessel Mirai in 2001. The first cruise, MR01/K02, was conducted from 14 to 28 May 2001 in the northwest Pacific near Japan. Lidar observations during the cruise were part of Japanese activities for the Asian Pacific Regional Aerosol Characterization Experiment (ACE-Asia) of the International Global Atmospheric Chemistry Program (IGAC). The second cruise, MR01/K05, was mainly concentrated in the western Pacific, including the tropics, from September to December 2001. Results presented in this study are from the first cruise; analyses of data from the second cruise are ongoing and will be reported in a companion paper. Figure 1 shows the cruise track of the MR01/K02; observations were made between 140°E and 160°E and 30°N and 40°N. Radar and lidar instruments were stored inside covered containers. The cover for the radar was made of Gore-Tex, and that of the lidar was glass. These covers were practically transparent for the sensors, so observations could be made continuously. The

cloud profiling radar, SPIDER, had a frequency of 95 GHz (wavelength of 3.16 mm) with a Doppler function and the ability to measure depolarization. Technical specifications of the radar are provided by *Horie et al.* [2000]. The radar reflectivity factor $Z_e$ was calculated as

$$Z_e(R) = \frac{\lambda^4}{\pi^5 |K|^2} \left[ \int \frac{dn(r,R)}{dr} C_{bk,ra}(r,R) dr \right] \quad (1)$$

where $\lambda$ is the wavelength, $K$ is a constant set at 0.828 in the analysis, $r$ is the radius of the particles, and $R$ is the altitude of the cloud layer of interest. $C_{bk,ra}$ is the backscattering cross-section of particles at $\lambda$ = 3.16 mm, and $dn/dr$ is the size distribution of the particles. The logarithmic form of radar reflectivity factor dBZe is often used. The original vertical resolution of the radar data was 82.5 m, and the maximum altitude of the observation was 12 km. Pulse reputation frequency (PRF) ranged from 500 to 800 Hz during the cruise. The minimum detectable radar reflectivity factor (dBZe) averaged over 1 min was −43 dBZe at 5 km. It is possible to infer cloud microphysics from the Doppler velocity of particles [*Matrosov et al.*, 1994] and the linear depolarization ratio (LDR; *Okamoto* [2002]). Here we concentrated on macroscale properties of clouds rather than microphysics, so discussions of Doppler velocity and LDR are not provided.

[9] *Sugimoto et al.* [2001] described technical specifications of the lidar, and *Sugimoto et al.* [2002] analyzed aerosol properties derived from the lidar data. The lidar for this study had three channels, two of which were for backscattering for copolarization at 0.532 $\mu$m and for co- and cross-polarization at 1.064 $\mu$m, respectively. The channels also allowed the measurement of depolarization capability at 0.532 $\mu$m. The original lidar data had a vertical resolution of 6 m and a temporal resolution of 1 sec. The maximum altitude of the observations was 20 km. The lidar backscattering coefficient $\beta_{true}$ is given in equation (2):

$$\beta_{true}(R) = \frac{1}{4\pi} \int \frac{dn(r,R)}{dr} C_{bk,li}(r,R) dr \quad (2)$$

where $C_{bk,li}$ denotes the backscattering cross-section at the lidar wavelength. In most cases, $\beta_{true}$ in equation (2) cannot be derived directly from lidar equations because attenuation due to molecules, clouds, and aerosols is large in the lidar signals. In general, corrections due to attenuation must be considered when inferring cloud microphysics from lidar data. These corrections were made for this paper using the attenuated backscattering coefficient $\beta_{obs}$, instead of $\beta_{true}$:

$$\beta_{obs}(R) = \beta_{true}(R) \exp(-2\tau(R)) \quad (3)$$

where $\tau(R)$ is the optical thickness at the lidar wavelength from the first layer to the layer at altitude $R$.

[10] Radar and lidar data were averaged so that vertical and temporal resolutions matched. The combined data used to study clouds included 159 vertical layers with a vertical resolution of 82.5 m. The minimum and maximum height were 0.6 and 12 km, respectively, and the time resolution was 1 min. Figures 2a and 2b show height-time cross-sections of the radar reflectivity factor and the lidar backscattering coefficient from 1.064 $\mu$m wavelength data for the whole period of the cruise. Data from 23, 24, and 27 May were excluded from Figure 2b to avoid noise in the lidar measurements that arose from heavy precipitation on those days.

## 3. Cloud Mask Schemes

[11] The received power is affected by particle size between the cloud and the radar or lidar such that the radar is sensitive to large particles and the lidar is sensitive to small particles. Furthermore, extinction due to clouds at lidar wavelengths is greater than extinction for radar. These differences affect how each sensor can be used and interpreted. How one sensor outperforms the other depends on macroscale properties of clouds and cloud microphysics as well as those of aerosols. Five different cloud mask schemes were used to assess how the radar and the lidar retrievals performed when clouds were present. The five schemes were (1) radar only, (2) lidar only, (3) both radar and lidar, (4) either radar or lidar and (5) second form of radar or lidar, where lidar is used to determine cloud bottom and remove the contamination due to drizzle appeared in radar signals. Therefore we describe the details of the cloud masks schemes in this section.

### 3.1. The Radar-Only Scheme (C1)

[12] The radar-only cloud mask scheme was a modified version of the scheme described by *Okamoto et al.* [2003]. If radar signals in two continuous layers are 0.2 dB above the noise level for the same time record, the two layers are recognized as cloud layers. Noise level is measured prior to the measurement of received power from each layer corresponding to each range in a record. The radar-only scheme was applied to observations for the whole observation period. This radar-only scheme was also tested for a case with clouds and precipitation, for example, for 18, 22, 23, 24, and 27 May 2001. For example, in the second half of the record for 18 May 2001, pixel noise levels increased above the cloud layers at around 6 km compared to cloud-free pixels at lower levels. Noise levels of pixels in the upper layers are affected by the "range side lobe" problem. When a strong return from a layer enters the receiver, received signals from upper layers are affected by the strong return such that the power level increases. Layers with higher noise level do not consist of cloud layers and should be considered to be cloud-free pixels. The radar-only cloud mask scheme works properly even in this situation.

### 3.2. The Lidar-Only Scheme (C2)

[13] The lidar-only scheme resembles the radar-only scheme. When lidar backscattering coefficients in two continuous layers exceed $10^{-5.25}$ [1/m/ster] at 1.064 $\mu$m, the layers are considered to be cloud layers. The threshold value is selected so that aerosols and noise are excluded. Lidar is more sensitive to small particles; it can therefore also observe aerosols. A threshold method for lidar data is important so that the cloud mask can eliminate pixels associated with aerosols. The lidar instrument has disadvantages in two situations. A lidar cannot penetrate thick clouds, so high cloud layers above thick clouds can be missed. In contrast, cloud radar will detect some of high clouds. Also, lidar cannot

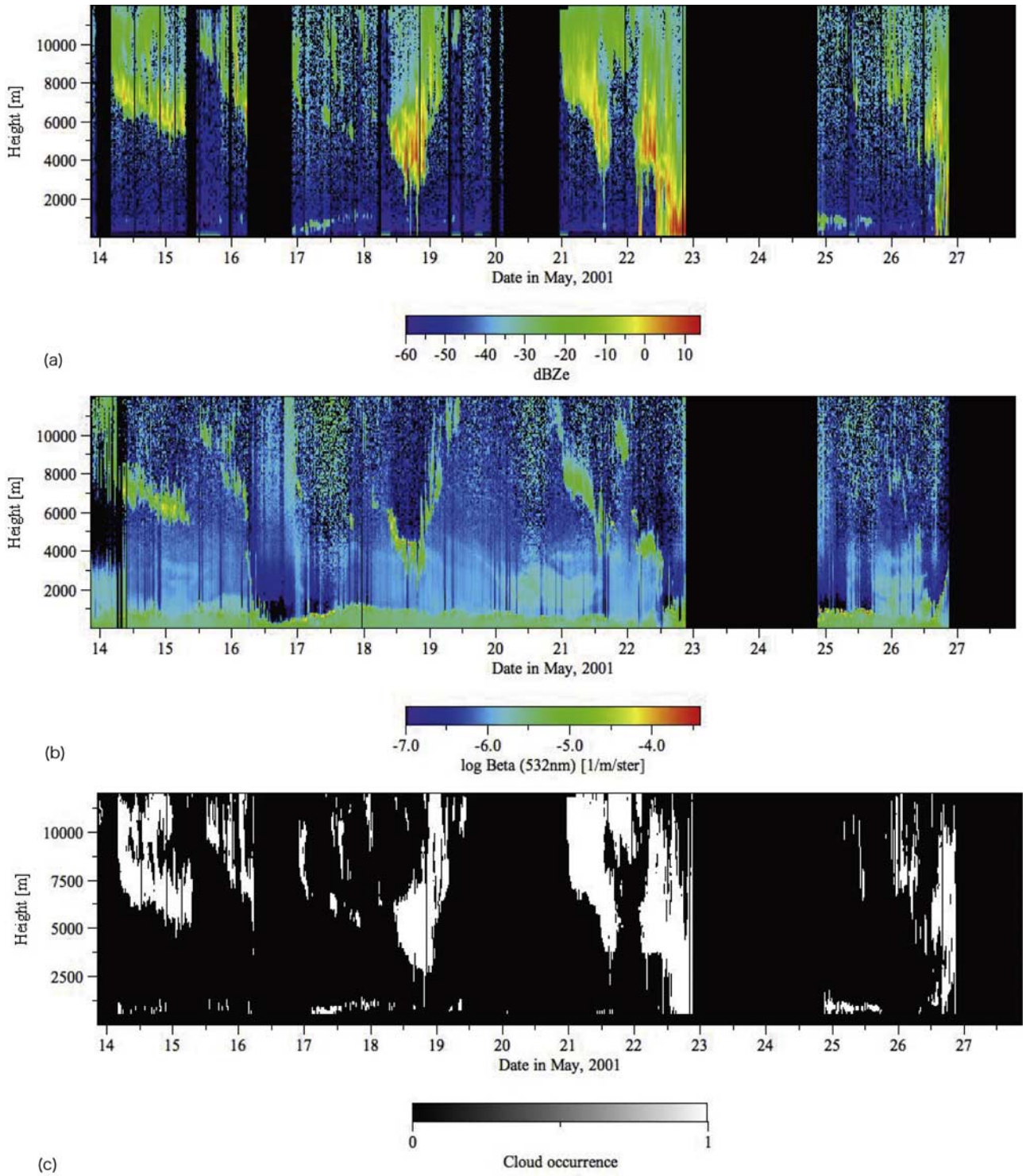


**Figure 2.** (a) Time-height plot of the radar reflectivity factor dBZe obtained by the 95-GHz cloud radar SPIDER during the Mirai cruise from 14–28 May 2001. (b) Time-height plot of the backscattering coefficient at 0.532 $\mu$m obtained by lidar. (c) Time-height cross section of cloud occurrence after the cloud mask scheme C5 based on radar or lidar for the whole observation period.

detect precipitation if there are so few precipitation particles that their optical cross section is smaller than the minimum detection limits of the lidar.

[14] The lidar can observe aerosol layers at or below 5 km, and cloud layers are detected within the aerosol layers. Lidar data complements the radar data in the detection of clouds, and the frequency of the low-level clouds is improved if lidar data are used. Many water clouds have large extinction cross-sections in lidar wavelengths, so the lidar can observe them. In contrast, backscattering cross sections of the same clouds in radar wavelengths are often smaller than the minimum detection limit.

### 3.3. Radar and Lidar Scheme (C3)

[15] In the "radar and lidar" scheme, if criteria for both schemes 1 and 2 as described in sections 3.1 and 3.2 are fulfilled, then the corresponding layers are considered to be clouds. Cloud frequency determined by this scheme is the lowest. The scheme is used in the retrieval algorithm of cloud microphysics [*Okamoto et al.*, 2003].

### 3.4. Radar or Lidar Scheme (C4)

[16] In the radar or lidar scheme, if criteria for either scheme 1 or 2 are fulfilled, the layers are recognized to be clouds. This scheme yields the largest cloud frequency of the four schemes when both sensors operate. However, it is difficult to separate precipitation from clouds in radar signals. Thus the scheme is used to estimate hydrometeor frequency, i.e., clouds and drizzles.

### 3.5. Second Form of Radar or Lidar Scheme (C5)

[17] The scheme C5 is similar to C4 except that the treatment of signals is different when temperature $T$ is above 0°C. According to *Hogan et al.* [2001], the lidar is considered to better sense cloud base. Here the lidar data is used to detect bottom of water clouds when $T > 0$°C, i.e., we remove the pixels detected by the radar below the bottom layer. That is, these removed pixels are considered to contain drizzle. For the layer higher than the cloud base and $T > 0$°C, C4 is applied to determine clouds. For $T < 0$°C, we also use C4. C5 is considered to be the most reliable cloud mask scheme and the difference between C4 and C5 is considered to correspond to the drizzle frequency of occurrence.

## 4. Cloud Occurrence

[18] Radar and lidar data can determine cloud frequency. Cloud detection during the cruise varied based on which of the five different schemes discussed in section 3 was used. The clouds had a multilayer structure. Analyses in the following sections excluded some data. Heavy precipitation was recorded on three days, (23, 24, and 27 May); therefore, the comparison of radar and lidar performance in cloud detection excluded data from those days. Only data from times when both sensors recorded observations were used. The five cloud mask schemes were applied to radar and lidar data during the period from 14–27 May 2001. Figure 2c shows the time-height cross section of cloud occurrence by C5.

### 4.1. Vertical Distributions of Cloud Frequency

[19] The number of cloud pixels at each height was counted in each of the five schemes to derive a vertical distribution of cloud frequency for each scheme (Figure 3a). More hydrometeors at low levels were detected by radar than by lidar; drizzle particles detected by the radar were not detected by lidar, and heavy precipitation events were

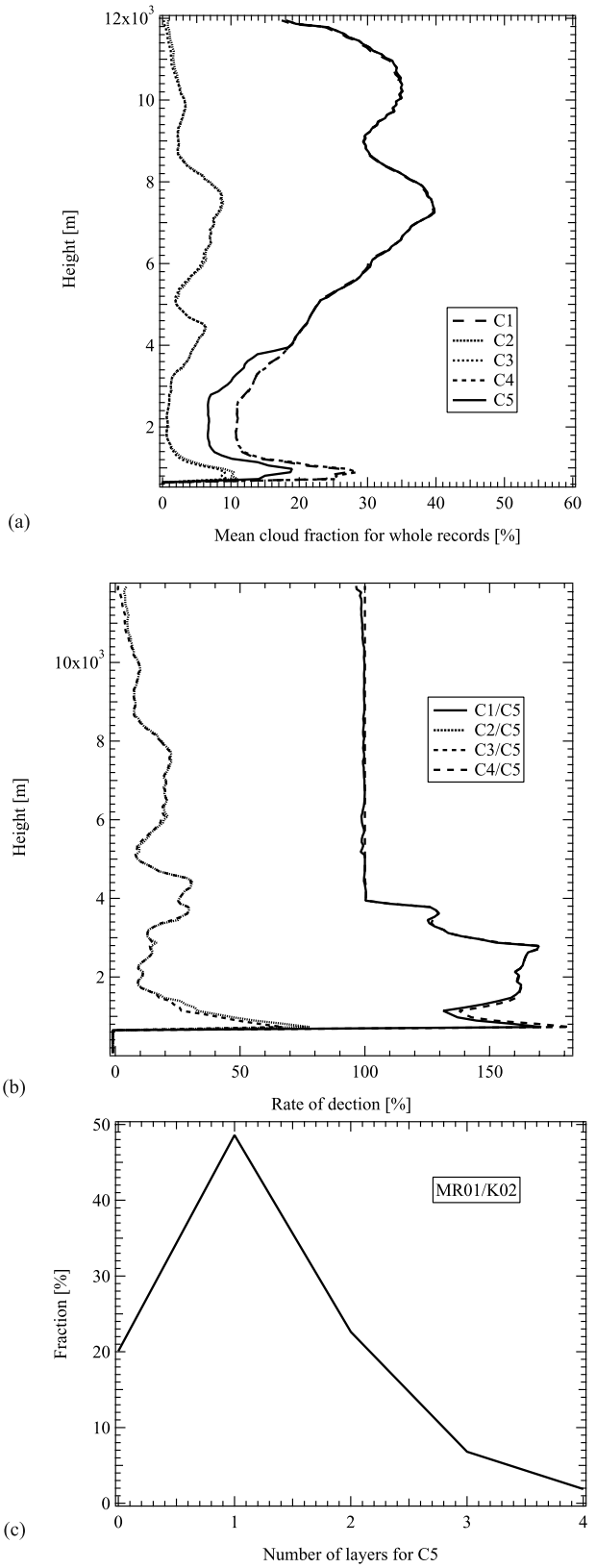


**Figure 3.** (a) Vertical structures of cloud frequency of occurrence averaged over the whole observation period based on the five cloud mask schemes, i.e., C1: radar only, C2: lidar only, C3: radar and lidar, C4 radar or lidar, and C5 second form of radar or lidar. For "radar and lidar" both sensor detected clouds, whereas for C4 "radar or lidar", at least one of the sensors detected clouds and for C5, the lidar detection of cloud bottom is introduced. (b) Performance of the radar and the lidar for cloud detection on the basis of C5 to be the reference solution. (c) Number of cloud layers averaged over the whole observation period derived from the cloud mask scheme C5.

excluded from this study. The difference between C4 and C5 at low level corresponded to the drizzle frequency of occurrence. C4 and C5 at 1 km were 29% and 19%, respectively. Thus the difference was about 10% at 1 km and the drizzle occurrence turned to be about one third of the frequency of occurrence of hydrometeors at the altitude. There were no differences between C4 and C5 for the layer >4 km since temperature was below 0°C and the schemes were actually the same in the height range. The difference between C5 and C1 denotes the improvement in detection that occurred when the lidar supplemented the radar above 4 km. The improvement was generally small: (C5−C1) for 12 km were 2%. At this level, the lidar was sometimes able to detect clouds that the radar could not, as radar sensitivity diminished above 10 km. The minimum detectable dBZe decreases as the altitude increases, yet small cloud particles can exist in upper layers. Such small particles may not be observed above a certain altitude by the radar alone because the radar loses sensitivity at that level. The difference between C5 and C2 denotes the improvement in detection that occurred when the radar supplemented the lidar. The lidar gradually loses the ability to detect clouds as altitude increases because of attenuation in the lidar wavelength.

[20] A detection rate is derived for each scheme based on the assumption that the vertical distribution of C5 best estimates the cloud frequency (Figure 3b). This detection rate helps assess the performance of both radar and lidar. For example, C1/C5 and C2/C5 estimate rates for radar-only and lidar-only schemes, respectively. Radar performance was excellent above 4 km. The radar identified more than 95% of the total clouds from 4 to 12 km. While, contributions from the lidar became very important below 4 km: C4/C5 was much larger than 100%. That is, the drizzle was effectively excluded from the radar echo by the cloud bottom information from the lidar. C4/C5 indicates the drizzle occurrences often exceed one third of the cloud occurrence during the cruise. The lidar detection of cloud bottom could be more important in the tropics where there is usually more precipitation activity than in midlatitude. In addition, subvisual clouds occur in the tropics above 15 km. Radar sensitivity is low at such high altitudes [e.g., *Heymsfield*, 1986]. In fact, *Iwasaki et al.* [2004] showed that only lidar could observe subvisual cirrus clouds during the Mirai MR01/K05 cruise in the tropics.

[21] The average vertical cloud structure during the cruise was characterized from these analyses as follows. Local maximum below 3 km occurred at 1 km and the cloud frequency was about 20%. Local maxima above 3 km occurred at 7.4 and 10.5 km, where cloud frequencies were 40 and 35%, respectively. A local minimum occurred at 9 km between the two maxima. These two maxima and the minimum correspond to the amount of relative humidity according to the radio-sonde measurements made during the cruise. A second local minimum in cloud frequency (7%) was around 2 km. These features were well reproduced by the radar-only scheme but cloud frequency derived only from the radar was biased below 4 km due to the drizzle. On the basis of the analyses for C4 and C5, the drizzle frequencies at 1 and 2 km were 9 and 4%, respectively. The rain gauge measurements were also carried out during the cruise and the precipitation frequency is derived. Here we applied a criterion of precipitation as the rain rate exceeds 0.5 mm/h. On the basis of the instrument, the frequency of precipitation during the cruise was found to be 2%. Therefore the derived cloud fraction here was not different from that for the records without precipitation recorded by the rain gauge.

[22] The value of 2% is much smaller than the one derived from the analyses of radar and lidar data. The difference in the frequencies between the rain gauge measurements and the active remote sensing attributes to the existence of drizzle that may not reach ground. Using the equation of droplet growth [e.g., *Rogers and Yau*, 1989], we estimated the evaporation time for given droplet radius, surface relative humidity and temperature. We considered the drizzle radius to be 50, 100, and 200 $\mu$m. Mean surface temperature and relative humidity are around 293 and 0.8 K, respectively, when drizzles are found by the radar and lidar during the cruise period. The evaporation time for 50 $\mu$m is estimated to be 50 sec. The fall speed of the particle is 0.4 m/s [e.g., *Rogers and Yau*, 1989]. The altitude of drizzle occurrence is found to be around 1 km. Thus the fall time is 2500 sec. In this case, the particle cannot reach the sea surface. For the particle of 100 $\mu$m, the evaporation time is estimated to be about 200 sec. The fall time is 1250 sec, estimated from the fall time of 0.8 m/s. The particle cannot reach the surface, too. The particle with 200 $\mu$m can be evaporated after 794 sec. The fall time is 625 sec. This particle may reach the surface. Since the typical radius of drizzle is around 100 $\mu$m, it is therefore concluded that most of the drizzle particle cannot reach before evaporation in this situation and thus the discrepancy between the drizzle frequency of occurrence derived from radar/lidar and the rain gauge can be explained by the evaporation of drizzle.

### 4.2. Number of Cloud Layers

[23] We investigated the average number of cloud layers for the same data as in section 4.1. The number of layers for each record were counted and averaged, and Figure 3c shows the results based on C5. The horizontal line is the actual number of layers, except that "four" represents four or more layers. The average number of layers was 1.23.

[24] Results from C5 could be used to characterize the properties of the multilayer structure. Probabilities of the occurrence of zero, one, two, three, and four or more layers were 20, 48, 23, 7, and 2%, respectively. If clouds existed in a region, the probability of multilayers, i.e., more than a single layer, was 32%. The average number of layers was 1.23 for all dates including those with clear sky. Cloud cover was estimated from the probability of a cloud with no layers subtracted from 100%. Thus, it was found a mean cloud cover of about 80% in the cruise data. The average number of layers (1.23) and the mean cloud cover (80%) yielded an average number of layers of 1.54 when clouds exist. The single layer assumption is usually made in retrieval algorithms for instruments, such as advanced very high resolution radiometer, moderate-resolution imaging spectroradiometer, or advanced earth observing satellite II. The cloud properties derived from these algorithms should be carefully tested against estimates from active sensors.

[25] *Wang et al.* [2000] analyzed statistics of annual mean cloud vertical structure from the 20-year radio-sonde data over the globe, land, and ocean. The frequency (%) of one,

two, three and four or more than four layered clouds are 58, 28, 9, and 5 over the globe and 63, 27, 7, and 3 over land and 56, 29, 10, and 5 over ocean. In a similar manner, we re-estimate the statistics from the Mirai cruise data by excluding the clear sky and the corresponding frequency (%) are 60, 27, 9, and 3. It is noted that the statistics from radio-sonde measurements have two problems, i.e., over-detect low-level clouds and miss 20–30% of high-level clouds, while radar/lidar observations is more robust, though the period and area of the Mirai cruise is much limited. Despite of these, the statistics of multilayered structure of clouds from these two different sources are somewhat very similar.

## 5. Validation of the General Circulation Model

[26] We compared the results of a general circulation model to radar and lidar data along the Mirai cruise track. Specifically, we focused on two comparisons: (1) cloud fraction and (2) radar reflectivity factor at 95 GHz and a lidar backscattering coefficient at 0.532 $\mu$m.

### 5.1. Model Description

[27] Comparisons were done using SPRINTARS, a model based on the CCSR-NIES GCM [*Takemura et al.*, 2000, 2005]. SPRINTARS can simulate the concentration of four types of aerosols such as sulfates, carbonaceous aerosols, sea salt, and dust, and this model has been used to assess the effects of aerosols on climate. The model in this study had T106 truncation, corresponding to a horizontal resolution of around 100 km, and 20 vertical levels. Time step was 8 min. Temperature, pressure, and relative humidity estimated in SPRINTARS were nudged with 6-hour interval NCEP/NCAR reanalysis data. Cloud and aerosol fields were generated using SPRINTARS. The convective clouds were simulated by the modified version of Arakawa-Schubert parameterization [*Arakawa and Schubert*, 1974], *Moorthi and Suarez* [1992]. Stratiform cloud was estimated by prognostic cloud water content by *Le Treut and Li* [1991]. The interaction of aerosol and clouds were taken into account only for water stratus clouds, i.e., a parameterization based on the Köhler theory is introduce to predict the cloud droplet effective radius (for further details of the schemes relevant to the above parameterizations, see *Ghan et al.* [1997] and *Takemura et al.* [2005]). SPRINTARS output compared in this paper included vertical distributions of water and ice cloud fractions ($CF_{raw}$), grid box mean liquid water content ($LWC_{gm}$), grid box mean ice water content ($IWC_{gm}$), effective radius $R_{eff}$ of water particles, and the extinction coefficients for the four aerosol types. $CF_{raw}$ is estimated from large-scale condensation parameterization, while $LWC_{gm}$ and $IWC_{gm}$ are estimated both from large-scale condensation and convective parameterization. The contribution of convective parameterization in $CF_{raw}$ is discussed later. Rain rate at 0 km for each time resolution is simulated as two-dimensional variable.

[28] The period of observation in this study was relatively short compared to previous studies, such as those of *Mace et al.* [1998a, 1998b] and *Hogan and Illingworth* [2000], which used ground-based radars. In this study, however, we compared climate model output with cloud radar and lidar observations made over the ocean.

### 5.2. Modeled Radar Reflectivity Factor in Cloud

[29] Prior to the comparisons of observed and modeled cloud fraction, it is necessary to estimate radar reflectivity factor and backscattering coefficient in cloud for wavelength of 1.064 $\mu$m in order to mimic the observational conditions.

[30] We first estimate LWC in cloud, $LWC_{in}$, from the parameters $LWC_{gm}$ and $CF_{raw}$.

$$LWC_{in} = \frac{LWC_{gm}}{CF_{raw}}. \quad (4)$$

Similar to $LWC_{in}$, we also estimated $IWC_{in}$.

[31] Then, the radar reflectivity factor in cloud, $dBZ_{e,in}$, water clouds was estimated using the similar look up tables (LUT) that are used in the radar/lidar retrieval method to derive microphysics [*Okamoto et al.*, 2003]. Here a lognormal size distribution function with the dispersion $\sigma = 1.5$ is assumed. Extinction and backscattering signatures at radar wavelength were calculated as a function of effective radius ranging from about 1 to 2000 $\mu$m for a constant values of $LWC_{in} = 1[g/m^3]$. Water cloud particles are assumed to be sphere and the Mie theory is applied to estimate the scattering signatures. And $LWC_{in}$ and $R_{eff}$ simulated by SPTINTARS were used to estimate $dBZ_{e,in}$. Attenuation due to lower clouds to the cloud of interest was also taken into account. Here cumulative optical thickness from the lower layers is estimated by using grid mean extinction. The maximum $LWC_{gm}$ was about 0.65 $g/m^3$. $R_{eff}$ for water ranged from 5 to 25 $\mu$m.

[32] Radar reflectivity for ice clouds was estimated using the two different approaches. One method uses a similar procedure as in water clouds where $IWC_{in}$ derived by $IWC_{gm}/CF_{raw}$ was used and $R_{eff}$ for ice particles was fixed at 40 $\mu$m (hereafter R40 model). The radius value was chosen because the value is used in SPRINTARS to calculate radiation due to ice clouds and the interaction between the radiation and cloud formation was involved in the simulations of SPRINTARS. Modified Gamma size distribution function with the dispersion $p = 2$ was assumed in the estimation of radar reflectivity for ice clouds. Ice is assumed to be sphere. Other approach used an empirical relation of $dBZ_e$ and IWC. In this study we used the Z-IWC relation by *Hogan et al.* [2001] where they derived the relation from 14 hours of in situ aircraft measurements in midlatitude for 95-GHz radar (hereafter HJI2001 model).

$$dBZ_{e,in} = \{\log_{10}[IWC_{in}] + 0.93949\}/0.0706 \quad (5)$$

where $dBZ_{e,in}$ is a logarithm form of radar reflectivity factor in cloud. It is noted that equation (5) is slightly different from the original one by *Hogan et al.* [2001]. This is because we use the different definition of radar reflectivity factor.

[33] It is noted that the model simulations allow the treatment of the water-ice mixed phase. Since $LWC_{gm}$ and $IWC_{gm}$ are separately simulated in the model as described in section 5.1 and are recorded as output values, it is enable us to separately estimate the radar reflectivity factor (and also lidar backscattering coefficient) for ice particles as well as those for water cloud particles. For the comparisons of these

simulated values with observed ones, the sum of radar reflectivity for ice and water is used.

[34] Finally, we considered the attenuation in radar reflectivity factor due to precipitation modeled in SPRINTARS. For model simulations, when the rain rate in the model simulation exceeds 0.5 mm/hour, the modeled radar signal was reduced due to the precipitation in the atmosphere and also due to absorption by the water particles attached on the redome, which is a cover of the container where radar is installed. *Iwasaki et al.* [2004] estimated the total loss due to precipitation in 95 GHz radar to be 11 dB in midlatitude from synergy measurement of 95 GHz cloud radar and 12 GHz radar held in Kashima in Japan. While the loss due to the water particles on the redome at 95 GHz was measured as about 9 dB in the laboratory experiment held in Kashima, Japan (H. Kuroiwa, private communication, 2001). Since the attenuation due to water vapor and precipitation in the atmosphere are about 1 or 2 dB, respectively, 11 dB loss determined by *Iwasaki et al.* [2004] is consistent with the value determined in the laboratory experiments. Consequently, when the model rain rate exceeded 0.5 mm/hour, the modeled radar reflectivity factor at that record was reduced by 11 dB. The attenuation due to rain increases with increasing rain rate, though the size distribution of precipitation particle may affect the absolute value. However, the effect of such variation in the attenuation is small. The attenuation due to precipitation can be considered to be smaller than the loss due to the water particles on the redome, which is 9 dB, by the following reason. As described in section 2, we already excluded the data in 23, 24, and 27 May where the rain rate often exceeded 1 mm/hour. Except for the 2 days, the rain rate rarely exceeded 1 mm/hour. Thus the attenuation due to precipitation is considered to be much smaller than 9 dB. For heavy precipitation events, the attenuation due to precipitation might become comparable or larger than the loss on the redome and more careful treatment of the attenuation is needed.

[35] t is noted that the simulated frequency of precipitation in the model is five times larger compared with the observed one, i.e., 11% and 2% for the model and the observations, respectively. The simulated cloud fraction and reflectivity factor for the whole records were actually different from those for the records without precipitation. Therefore it is important to include the effect of loss due to the precipitation.

### 5.3. Modeled Lidar Backscattering Coefficient in Cloud

[36] Lidar signals can be simulated from SPRINTARS output, and contributions from both aerosols and clouds should be considered. Lidar backscattering $\beta_{\text{true}}$ given in equation (2) was computed at a wavelength of 1.064 $\mu$m from the extinction coefficient for each aerosol type using the mode radii in the model. In the simulations, the extinction coefficients for the four types were converted to the lidar backscattering coefficients with help of the aerosol size information in SPRINTARS where hygroscopic growth effects for sulfate and carbonaceous aerosols were considered according to the value of the relative humidity in the grid box. The optical properties of molecular scattering were calculated using the midlatitude summer model published by *McClatchey et al.* [1972]. For the estimation of backscattering coefficient by ice clouds, we only used R40 model. Since HJI2001 model can only be directly applied to radar reflectivity, we have not used it for the simulation of lidar backscattering. Effect of multiple scattering for water clouds was taken into account on the basis of the backward Monte Carlo simulation [*Ishimoto and Masuda*, 2002] where the contribution of multiple scattering is parameterized by the function of effective radius and $\text{LWC}_{\text{in}}$. The total lidar backscattering coefficient was calculated as the sum of the backscattering coefficients for four aerosols and water and ice clouds. Finally, the attenuated backscattering coefficient $\beta_{\text{obs}}$ given in equation (3) that resulted from aerosols and clouds was computed, where attenuation in the lidar signals due to extinction from modeled aerosols and clouds was fully considered for the comparisons.

### 5.4. Cloud Fraction Comparisons

[37] Observed cloud fraction was estimated from the cloud occurrence C5 that was based on the second form of radar or lidar scheme. Cloud occurrence was averaged with a time step of 1 min over 6 hours. Only those data observed when both radar and lidar functioned were used in this example to derive the cloud fraction. If a grid box was considered to be cloudy by the scheme, the cloud fraction in a grid box was 100% for 1 min to allow estimates of cloud fraction for a pixel with time resolutions of 6 hours.

[38] Estimation of modeled cloud fraction was carried out as follows. Radar signals for some high clouds were associated with low values of $\text{IWC}_{\text{in}}$ or small particle radii that were below the minimum detectable radar signals shown in Figure 4a. If the simulated radar signals in cloud in the SPRINTARS model exceeded the minimum detectable radar reflectivity at that altitude or the modeled lidar backscattering coefficient in cloud exceeded $10^{-5.25}$ [1/m/ster] at 1.064 $\mu$m as done in the estimation of observed cloud by C5, the cloud fraction was included in the comparisons. In addition, when temperature was higher than 0°C, the cloud bottom was determined by the lidar in a similar manner as C5, i.e., pixels below the bottom are considered to be cloud-free. When a model grid box contains clouds, the cloud fraction for the box was taken to be the same value as the original output. If the simulated signals in cloud do not exceed the radar sensitivity value, the cloud fraction in that pixel was set to 0. Since the radar sensitivity was introduced in the detection of clouds in the model simulations for the comparisons, it is instructive to know the minimum detectable IWC. The minimum detectable IWC can be estimated using the minimum detectable radar reflectivity factor (Figure 4b). R40 and HJI2001 models show the minimum $\text{IWC}_{\text{in}}$ at 8 km to be about $10^{-4}$ and $2 \times 10^{-4}$ g/m$^3$, respectively. When there was no cloud below a grid box of interest, i.e., no attenuation, and the modeled $\text{IWC}_{\text{in}}$ in the box was below the minimum detectable IWC at the altitude of the box, the box was treated as cloud-free one unless the lidar signal in cloud was larger than the threshold value for cloud mask.

[39] Figure 5a showed the height-time plot of cloud fraction from the observations. Figures 5b and 5c showed the corresponding cloud fractions estimated by SPRINTARS with R40 and with HJI2001 ice model, respectively. It should be noted that the model results were also shown for the data below 0.6 km. There were water clouds below 0.6 km in the model. The results of the two models were

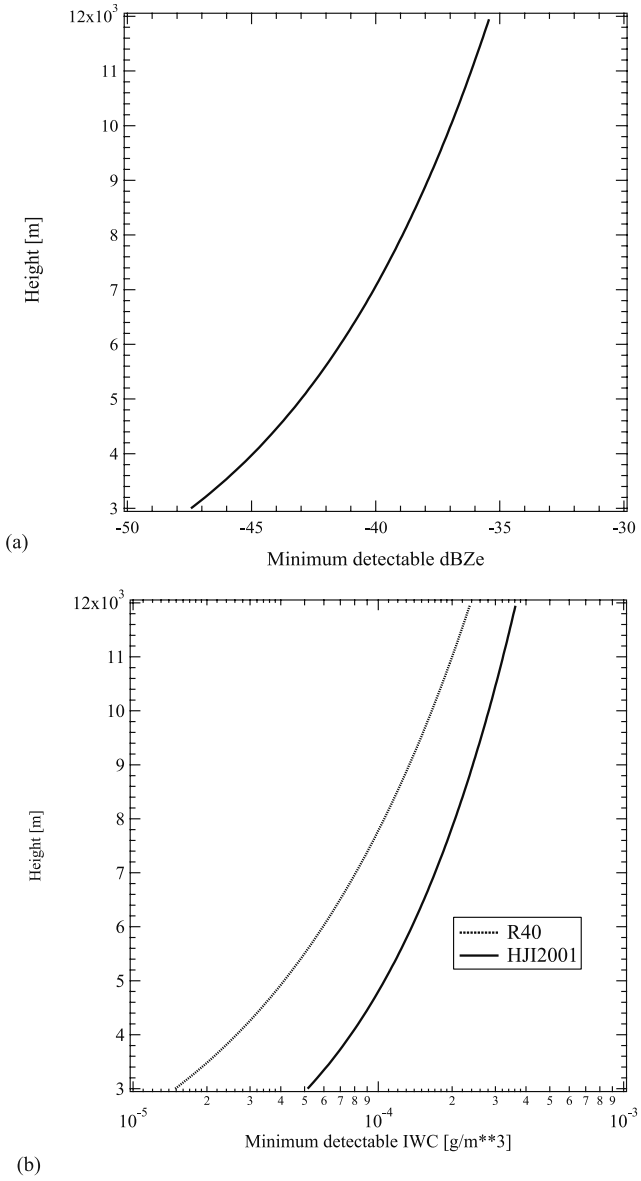


**Figure 4.** (a) Minimum detectable radar reflectivity factor. (b) Minimum detectable ice water content (IWC) for SPRINTARS with R40 and HJI2001 models.

similar except for the region above 9 km where the cloud fraction for HJI2001 model was slightly larger than that for R40. We first compared the modeled and observed cloud occurrences (Figure 5d), where we used R40 model since there is only a small difference between the two model simulations. Cloud occurrence in the model was determined by the cloud mask scheme. Red, yellow, green, and blue colors correspond to (1) both did not show clouds (also indicated by blue), (2) only observation showed cloud (green), (3) only GCM produced clouds (yellow), and (4) both of the observation and the GCM produced clouds (red), respectively (Table 1). The cloud fraction pattern from the two models resembled the observations as indicated by red color, but the model predicted more cloud occurrence than observed above 8 km seen by yellow and less cloud occurrence below 8 km as seen by the green. For grid boxes where both the observation and the model showed the cloud occurrence, we further examined the difference of the cloud fraction between the observation and the model. Figures 5e and 5f showed the area where cloud fraction simulated by the SPRINTARS (R40) was larger than that by the observations based on the C5 cloud mask scheme and the area where the model underestimated cloud fraction, respectively. It turned out that the overestimation of cloud fraction in the model occurred in upper portion of clouds >8 km and the underestimation occurred in lower altitude when cloud occurrence predicted correctly in the model.

[40] These results were somewhat similar to the findings by *Mace et al.* [1998a] and *Hogan and Illingworth* [2000]. The model also predicted fewer clouds than observed below 2 km. The model failed to predict some fraction of the water clouds around 1 km that were detected by the observations.

[41] Figure 6 shows the vertical distribution of mean cloud fraction as observed and modeled above 0.6 km. Mean cloud fraction from observations was the same as the averaged cloud frequency derived using the cloud mask scheme C5 in section 4. The mean cloud fraction predicted by SPRINTARS was the average of the cloud fraction for each 6-hour interval during the period above. There are three simulated cloud fractions, i.e., the original cloud fraction that ignored radar sensitivity, the results by R40 model, and the results by HJI2001 model. The differences between the three simulations are small. The discrepancies were found above 10 km and the difference between the original and R40 cloud fractions was about 5% at 11 km. The R40 and HJI2001 models gave similar results, though R40 model produced the smallest fraction. It was concluded that the radar sensitivity had a relatively small effect on the estimation of cloud fraction in the cruise data because most signals in model simulations exceeded the sensitivity value and were larger than observed reflectivity.

[42] Cloud occurrence below 2 km was underestimated in part because of deficiencies in water cloud prediction of the model. The local minimum of mean cloud fraction in the model simulations was located at about 0.6 km and was below that of observations, i.e., 2 km. In contrast, to the comparisons at lower altitudes, the model significantly overestimated mean cloud fraction above 8 km. Observations showed local maxima in cloud fraction at 7 and 10.5 km. The model did not predict these local maxima. Instead, mean cloud fraction in the model increased with altitude. Overprediction of upper clouds may attribute to deficiencies in the model cloud scheme such as the underestimation of terminal velocity of ice particles, leading to the longer lifetime of the clouds.

[43] *Mace et al.* [1988a, 1988b] made similar comparisons of cloud occurrence and examined fractional differences between observations and model simulations for data over Oklahoma in winter of 1997. They showed that the frequency of hydrometeors in the ECMWF model was greater than observed in upper layers and suggested that such overestimates in the model arose because the model predicted layers that were too deep and dissipated later than observed. *Hogan et al.* [2001] investigated mean cloud frequency and mean cloud fraction for data at Chilbolton, southern England, between 24 October 1998 and 23 January 1999. The ECMWF under-predicted cloud fraction between 1 and 7 km. The ECMWF overpredicted mean cloud fraction above 8 km. Inclusion of snowfall improved the

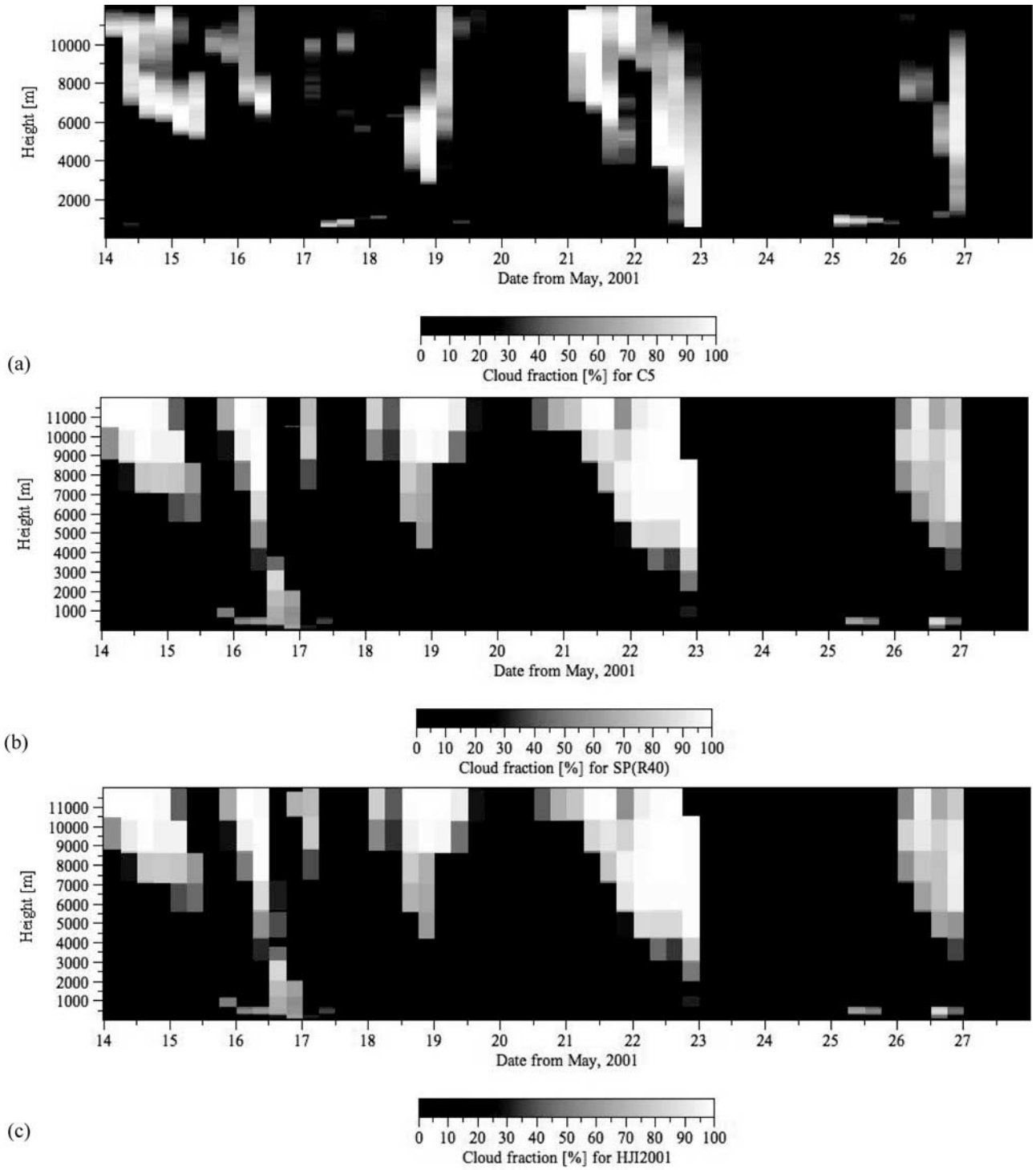


**Figure 5.** (a) Height-time cross section of cloud fraction derived from the radar and lidar observations. (b) Same as Figure 5a, but from the SPRINTARS with R40 model. (c) Same as Figure 5a but from the SPRINTARS with HJI2001 model. (d) Height-time cross section of type for cloud occurrence based on the comparison of cloud fraction from observation with C5 scheme and that from SPRINTARS with R40. The number (color) in the figure is defined in Table 1. (e) Height-time cross section of the differences of cloud fraction between the SPRINARS with R40 model and the observations. The area of overestimation in the model was shown. (f) The same as Figure 5e for the underestimation in the model.

agreement with observations, although mean cloud fraction was still underestimated below 750 m. These model results were similar to results in our study using SPRINTARS, with some discrepancies. The ECMWF model overestimated mean cloud fractions above 8 km, but both the ECMWF and observations showed a decrease in cloud fraction with increasing altitude. Similarly, both observations and the ECMWF showed local maxima in cloud fraction between

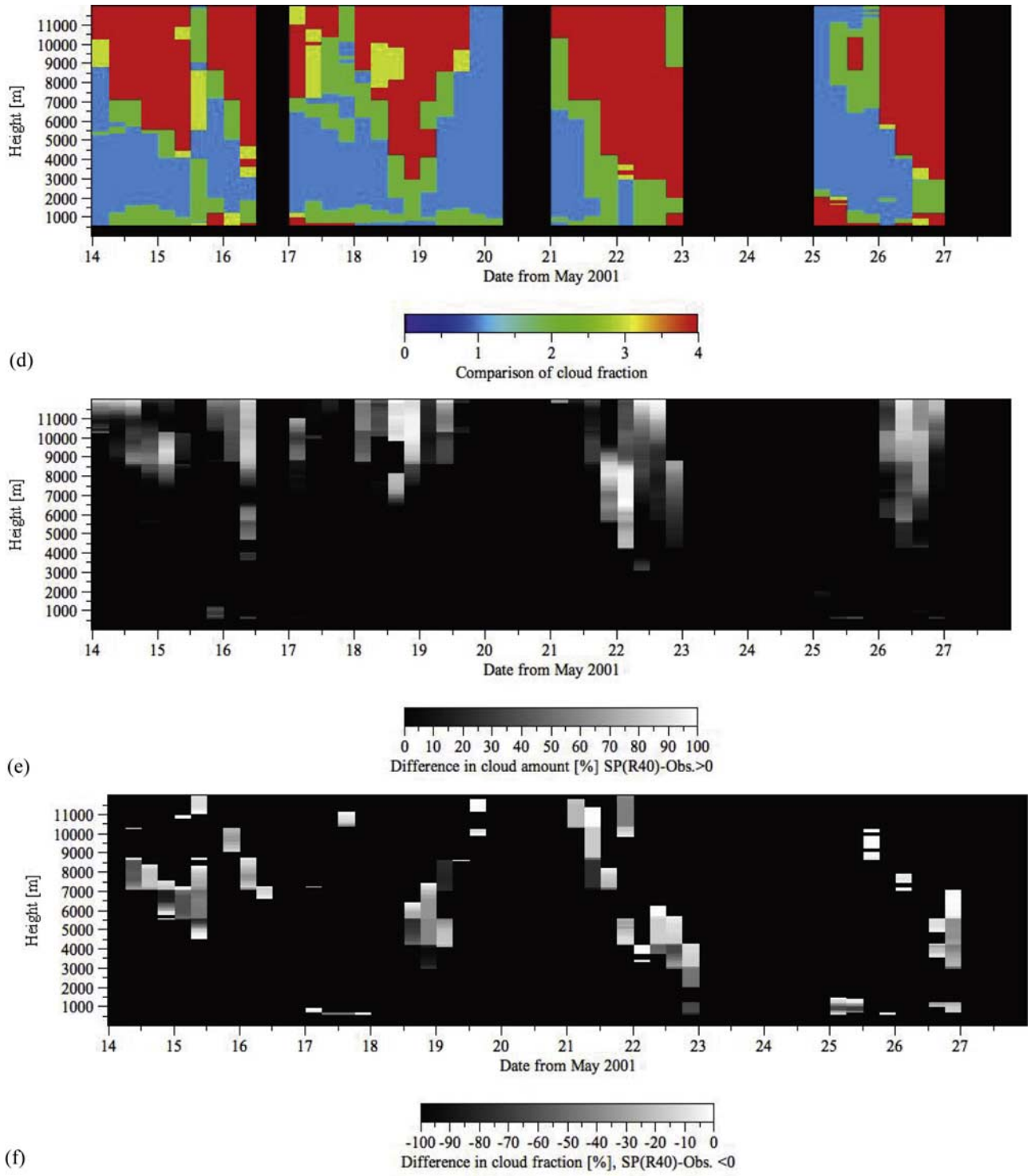


**Figure 5.** (continued)

5 and 8 km. In contrast, SPRINTARS failed to predict two local maxima in cloud fraction at 7 and 10.5 km and instead showed a steady increase in mean cloud amount as altitude increased above 8 km. Consequently, differences between the SPRINTARS and observations increased with altitude. Mean cloud fraction in our study was larger than in the study by *Hogan et al.*, for example, 35% (this study) versus 10% [*Hogan et al.*, 2001] at 10 km. It is unclear whether discrepancies in mean cloud fraction between the ECMWF

**Table 1.** Classification of Type for Cloud Occurrence Comparison Between the Model and Observation[a]

| | No (Observation) | Yes (Observation) |
|---|---|---|
| No (SP) | 1: Blue | 2: Green |
| Yes (SP) | 3: Yellow | 4: Red |

[a]"No" denotes that there is no cloud detected and "yes" denotes cloud is detected. for example, "4 (red)" denotes the both model and observation show there is a cloud in the grid box.

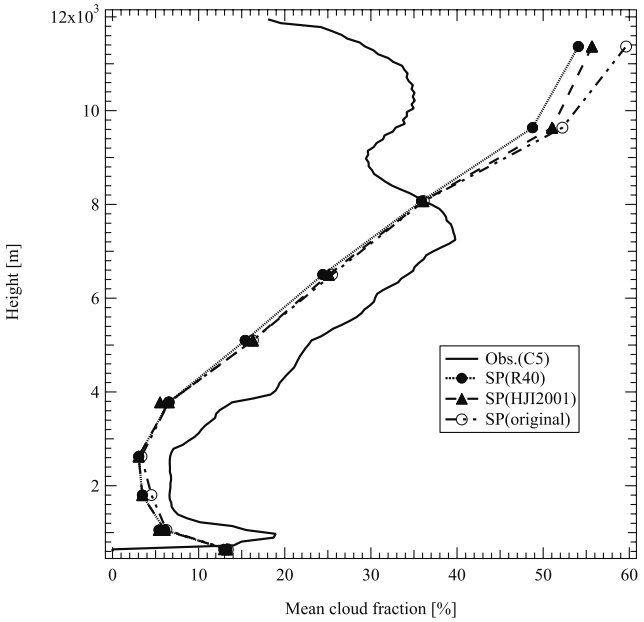


**Figure 6.** Comparison between averaged vertical profiles of mean cloud fraction deduced from radar or lidar data and from SPRINTARS.

and the observations are larger or not when the ECMWF model is applied to situations with large cloud fractions in upper layers.

[44] Similar to the approaches by *Hogan et al.* [2001], frequency distribution of cloud fraction in observations and the models were investigated in the three different height categories bounded 3 and 7 km. Ten cloud fraction bins were used and the value of cloud fraction bin denotes the midpoint of the bin, for example, cloud fraction bin of 15% represented the data between 10 and 20%. The frequency distributions of the simulated cloud frequency of occurrence were almost identical between the R40 and HJI2001 models for the low cloud (Figure 7a). This was because there were only a few ice clouds in this height range. The model shows overestimation of clouds with small cloud fraction (<10%) than observed one. It is noted that cloud fraction for 5% bin contained data for 0 %, i.e., clear sky data. It was found the models under-estimated the frequency from 15 to 45% bin. Above 45% bin, simulated frequency distribution of cloud fraction agreed with the observations. The difference became larger for large cloud fraction e.g., the model underpredicted clouds with 95% bin.

[45] The situation was similar in middle cloud. The frequencies for small and very large cloud fraction bins were over and under predicted in the model. The frequency for moderate cloud fraction bin was reasonably well reproduced in the model (Figure 7b). The result of the comparisons in high clouds was very different from those for the other two height categories. The model under-predicted frequencies for cloud fraction bins <65% and significantly overpredicted cloud with its amount of 95% bin (Figure 7c). This caused the overall overestimation of mean upper cloud fraction in high-level cloud as already found in Figure 6.

[46] In our GCM simulations, $LWC_{gm}$ and $IWC_{gm}$ were actually estimated from both large-scale condensation and convective parameterization. While cloud fraction, $CF_{raw}$,

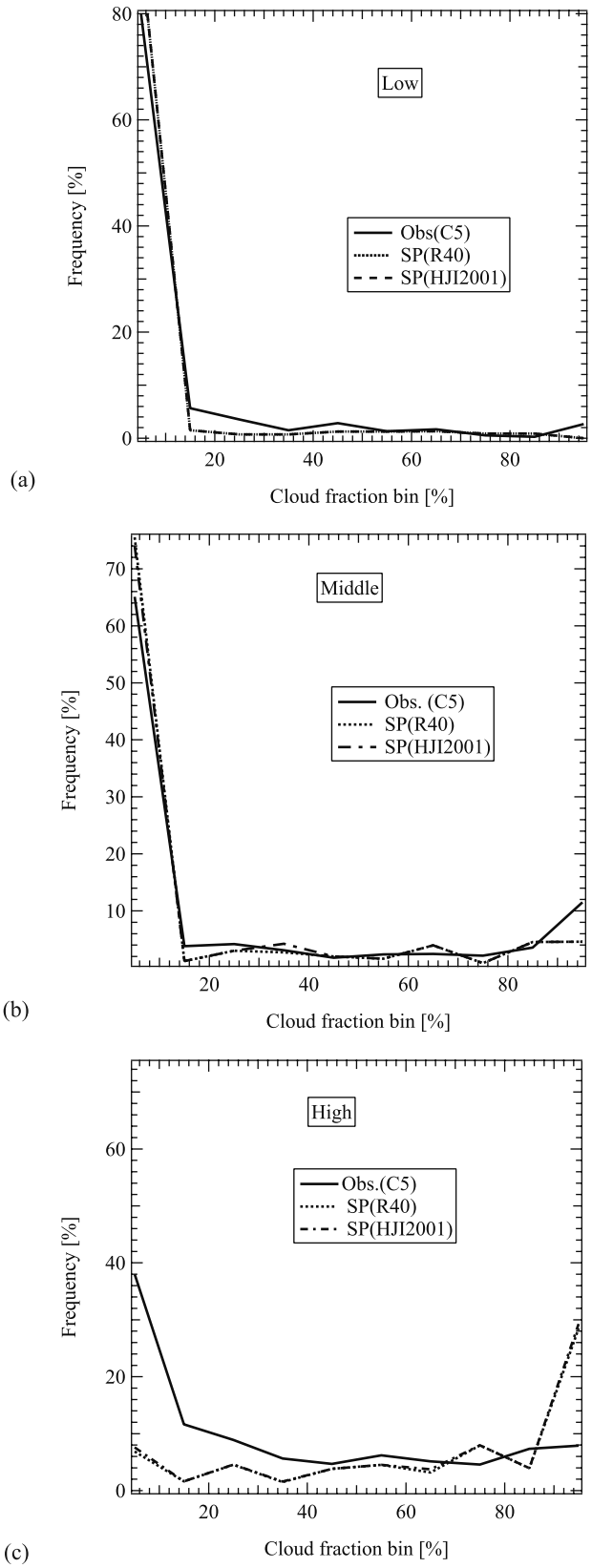


**Figure 7.** Comparison of frequency distribution of cloud fraction from the observations and two SPRINTARS in the three different height categories bounded 3 and 7 km. (a) Low cloud, (b) middle cloud, and (c) high cloud.

used in this study was estimated only from large-scale condensation parameterization. Although the cloud fraction from convective parameterization is originally two-dimensional variable, the contribution of cloud fraction from convective parameterization may be taken into account in the estimation of total cloud fraction $CF_{TOT,raw}$, which is three-dimensional variable.

$$CF_{TOT,raw} = 1 - \left(1 - CF_{LS,raw}\right)\left(1 - CF_{CU,raw}\right) \quad (6)$$

Where $CF_{LS,raw}$ denotes the cloud fraction for large-scale condensation parameterization, which is three-dimensional variable, and is actually used as $CF_{raw}$. $CF_{CU}$ is cloud fraction for convective parameterization and is the two dimension variable. It is noted that the contribution of convective parameterization is taken into account only for the case of nonzero cloud water or ice water from convective parameterization. Then, we perform the same procedure to obtain the ''observed'' total cloud fraction $CF_{TOT}$ to take into account the sensitivity of instruments except that the cloud fraction is now based on the $CF_{TOT,raw}$, instead of $CF_{LS,raw}$. $CF_{TOT}$ is found to be almost identical to the cloud fraction only for large-scale condensation parameterization. Therefore the discussions related to the modeled cloud fraction remain the same.

[47] There were uncertainties in the estimation of observed cloud fraction due to the finite transect. The uncertainties may arise from the sensitivity of the instruments, which is determined by the vertical resolution, as well as the cloud properties. In order to consider the former issue, we introduced the observed cloud fraction as a reference for the validation of model cloud fraction by applying the same sensitivity of the instruments in the observations, instead of the observed cloud fraction being truth. The uncertainty might also exist in horizontal direction when the comparisons are tried between observation and model [*Astin et al.*, 2001]. However, since most of the comparison between model and observation for each comparison timescale show the similar tendency of the model during the whole cruise period, i.e., over/under estimation of upper/lower cloud fraction in the model, we believe the problems in the model actually exist.

### 5.5. Comparisons of Grid Mean Radar and Lidar Signals

[48] Comparisons of the radar reflectivity factors and the lidar backscattering coefficient facilitate the validation of model cloud microphysical properties such as LWC/IWC and $R_{eff}$. In situ measurements and remote sensing techniques are often used to validate these parameters. For remote sensing, retrieval algorithms can use data from active and passive instruments. The combination of radar and lidar data is a powerful tool to help retrieve ice microphysics [*Okamoto et al.*, 2000, 2003; *Donovan an van Lammeren*, 2001; *Wang and Sassen*, 2002]. Applicability is limited for ground-based measurements to cases in which there are no water clouds below the ice clouds of interest. Section 4 showed that the probability that the radar and the lidar can record the same clouds was 20% at 8 km and 10% at 10 km. That is, the remaining clouds may not be analyzed by the radar/lidar method. Similar limitations exist in the LIRAD method that uses lidar and an infrared radiometer [e.g., *Platt*, 1973]. A radar using a multiparameter technique [*Matrosov et al.*, 1994], for example, a reflectivity and Doppler velocity, has wider applicability especially to optically thick clouds than a radar and lidar method, although the removal of vertical air motion in the Doppler velocity is an issue and the retrieval errors must be verified. We did not use retrieval algorithms in this study. Instead, radar and the lidar signals were simulated from SPRINTARS output and directly compared to observations as an alternative approach to validate cloud microphysics in the model. Contrary to the studies of cloud fractions where we used radar and lidar signals in cloud, the grid mean radar and lidar signals were simulated in the subsection.

#### 5.5.1. Grid Mean Radar Reflectivity Factor

[49] Radar reflectivity was averaged for 6 hours from the original radar data, which has a time resolution of 1 min, to enable a comparison of model results with observations. The parameters $LWC_{gm}$, $R_{eff}$, and cloud fraction were used to estimate the radar reflectivity factor for water clouds simulated by SPRINTARS. Radar reflectivity for ice clouds was estimated using a similar procedure that uses $IWC_{gm}$, $R_{eff}$, and cloud fraction. The maximum $LWC_{gm}$ was about 0.65 g/m$^3$. $R_{eff}$ for water ranged from 5 to 25 $\mu$m. The maximum $IWC_{gm}$ was 0.15 g/m$^3$. Here we estimated two modeled radar reflectivity for grid mean, i.e., one for R40 model where $R_{eff}$ for ice particles was fixed at 40 $\mu$m and the other for HJI2001 model as in the comparison of cloud fraction. Prior to the estimation of grid mean signals, we needed to estimate radar and lidar signals in cloud in order to taken into account the sensitivity of the instruments and effect of attenuation due to precipitation.

[50] It is noted that there was no difference in the estimation of radar reflectivity due to water clouds between the two model simulations as in the cases for the signals in cloud. The model allowed a mixture of water and ice clouds within the same grid box. During the period of observations, the maximum height of water clouds in the model was around 7 km; the minimum height of ice clouds was 4.5 km. Only ice clouds occurred above 7 km and only water clouds occurred below 4.5 km in the model. Water and ice clouds coexisted in the model between 4.5 and 7 km on 16, 18, and 22 May. This highlights the difficulty in directly comparing model microphysics with the retrieval results.

[51] Figures 8a and 8b show height-time plots of radar reflectivity observed by the radar and predicted by SPRINTARS with R40 model. The $dBZ_{e,gm}$ pattern simulated by the models agreed with observations as expected from the cloud fraction comparison (Figures 5a and 5b). Radar signals mainly reflected patterns of $R_{eff}$, rather than $LWC_{in}/IWC_{in}$, in addition to the cloud fraction. Ice clouds in the R40 model had a constant effective radius, so the pattern of estimated $dBZ_{e,gm}$ resembled that of cloud fraction in the model. Cloud fraction was often smaller near the cloud bottom compared to the upper parts of the cloud. Thus, the model $dBZ_{e,gm}$ at the bottom of the cloud was not necessarily smaller than values in the upper part of the cloud, for example, on 14 May. In contrast, observed $dBZ_{e,gm}$ was usually larger near the cloud bottom. In order to see the differences between the observed and modeled $dBZ_{e,gm}$, the time-height plot of differences for the overestimation and underestimation in the model were shown in Figures 8c and 8d. These comparisons were made for the grid where both

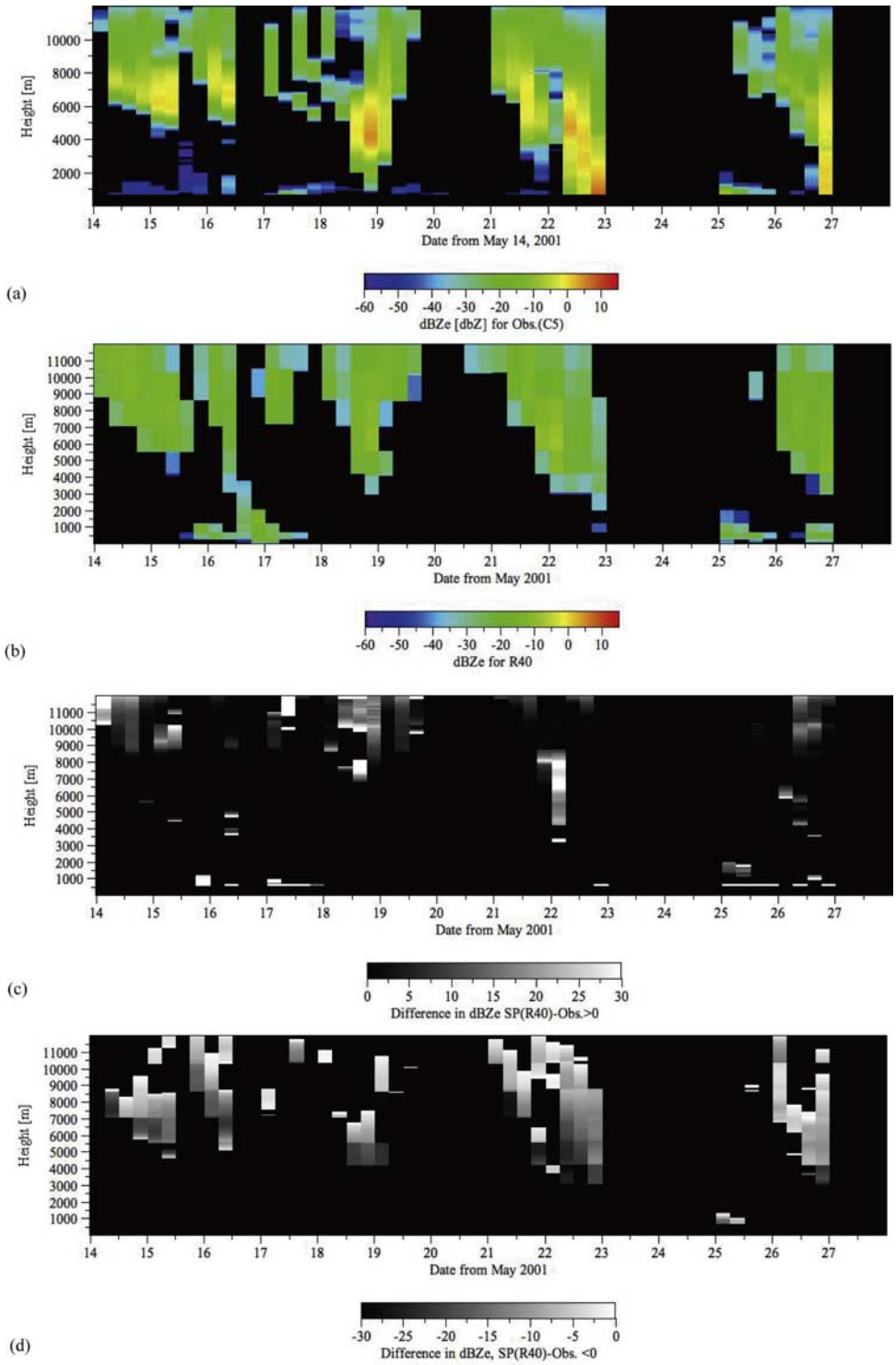


**Figure 8.** (a) Height-time cross section of the grid mean radar reflectivity factor dBZe averaged over 6 hours from the radar observations. (b) Same as Figure 8a, simulated by the SPRINTARS with R40 model. (c) Difference in dBZe between the SPRINTARS with R40 model and the observation. Only the positive value of the difference is shown. (d) The same as Figure 8c but for negative value. (e) Same as Figure 8b but for the SPRINTARS with HJI2001 model. (f) The same as Figure 8c but for HJI2001 model. (g) The same as Figure 8d but for HJI2001 model.

observed and modeled cloud fraction were larger than 0 after the application of the cloud mask. It was found that the model $dBZ_{e,gm}$ near the cloud bottom was smaller than observed, as on 15, 18, 24, and 26 May. This indicated that the radius assumed in the model was smaller than observed near the cloud bottom. The model $dBZ_{e,gm}$ due to water clouds was overestimated compared with the observations, suggesting simulated radius of water particles to be larger

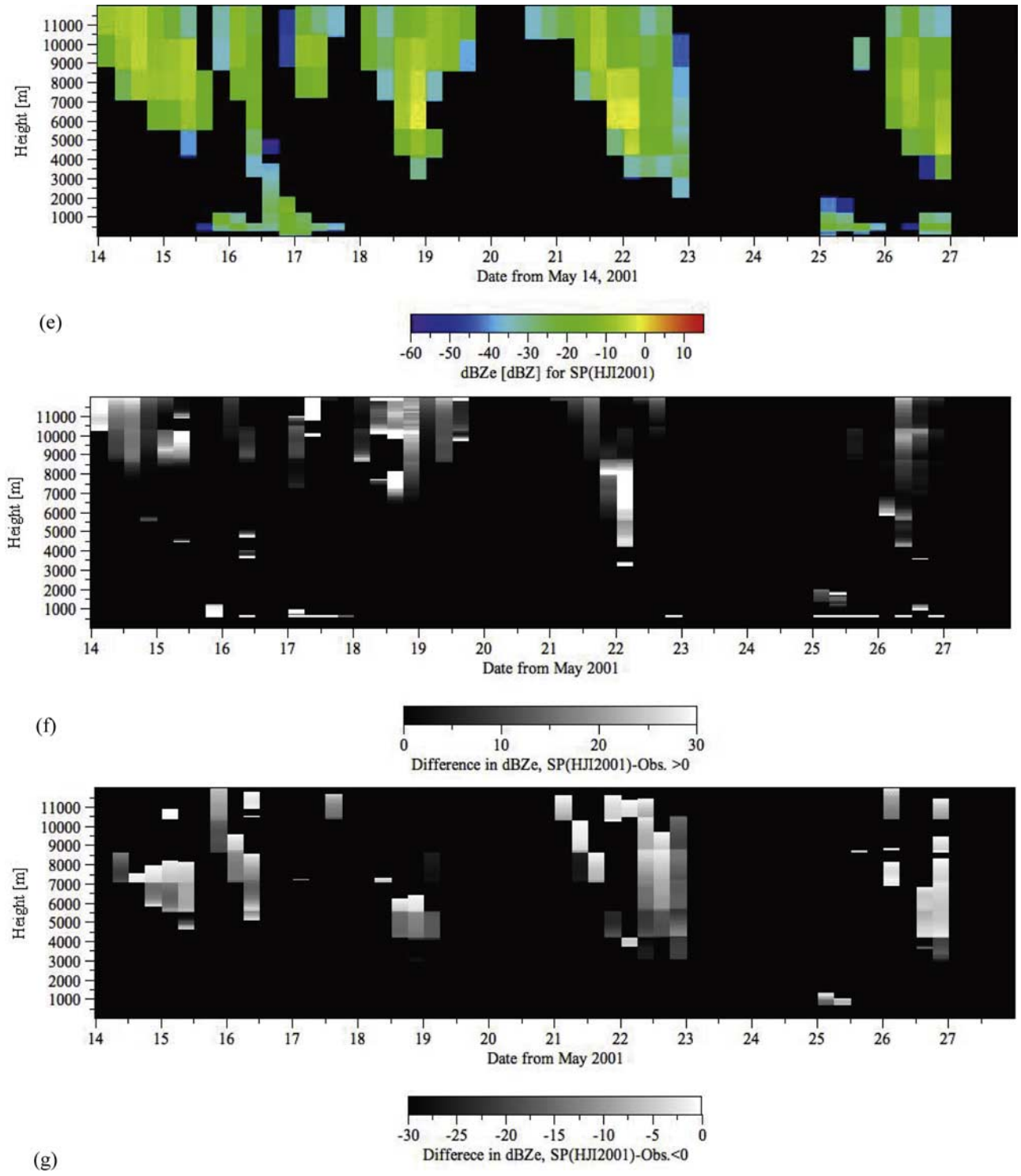


**Figure 8.** (continued)

than the actual one. The similar comparisons were performed between the HJI2001 model and the observations. Figure 8e showed the time-height plot of $dBZ_{e,gm}$ for HJI2001 model. The simulated $dBZ_{e,gm}$ for HJI2001 model was larger than that for R40 model at above 5 km. And the general pattern of differences between the simulated $dBZ_{e,gm}$ for HJI2001 and observed one was quite similar to the one between R40 model and the observations (Figures 8f and 8g).

[52] We then compared the vertical distribution of mean $dBZ_{e,gm}$ between observation and the two models in Figure 10a. Below 8 km, the models underestimated reflectivity. That is, the models certainly under-predicted radii of cloud particles and overpredicted above 10 km where both models overestimated $dBZ_{e,gm}$. The radar reflectivity is mostly affected by the particle size. Thus, the under/over estimation of reflectivity in the middle/high level clouds suggested the under/over estimation of particle size.

[53] There were different features in the two models. HJI2001 model gave larger radar reflectivity than the R40 model above 4 km. And above 8 km, the HJI2001 model gives larger value compared with the observed one, while R40 model underestimated it below 10 km and overestimated it above 10 km. Although we used lidar information in order to exclude drizzle and precipitation below cloud bottom, the lidar signal often exceeds the threshold value used in the C5 cloud mask when the precipitation becomes strong. In such cases, the radiative impact due to the large amount of the water content should become important and since the model does not take into account the radiative effects, the underestimation of the reflectivity below 4 km illustrated the deficiency in the estimation of radiative effects in the model.

#### 5.5.2. Grid Mean Lidar Signals

[54] There may be several approaches to compare the lidar signals between the observation and the models, for example, signals due solely to aerosols, due to aerosols and clouds, and due solely to clouds, etc. Since we were interested in cloud properties in the study, the lidar signals due to clouds were examined here. Observed lidar backscattering coefficient due to clouds was determined by application of cloud mask scheme C5 as in radar reflectivity. Similar procedure in the estimation of grid mean radar signals were applied in the estimation of grid mean lidar signals, for example, we first estimated the radar reflectivity and the lidar signals in cloud and then applied the cloud mask. At this point, the grids only containing aerosols were excluded. Consequently, the grid mean lidar signal due to clouds at 1.064 $\mu$m was estimated.

[55] Figures 9a and 9b shows lidar backscattering coefficients in grid mean as observed and simulated above 0 km. As might be expected given the radar comparison, observed lidar patterns agreed with the model, at least near the cloud bottom above 3 km. On 16, 17, 22, and 26 May, simulated lidar signals were strongly attenuated, whereas actual observations were less attenuated. It was obvious that the model extinction was overestimated in water clouds; that is, there were too many cloud particles. Then we investigated the difference between the observed and simulated $\beta_{gm}$ when both observation and simulations show the cloud occurrence in a same grid box (Figures 9c and 9d for over- and underestimation of $\beta_{gm}$ in the model, respectively). The model overpredicted $\beta_{gm}$ at cloud bottom and significantly underpredicted it above cloud bottom layer. This may attribute to the over estimation of extinction in the lower part of clouds. Then comparisons of the observed and model mean $\beta_{gm}$ were done (Figure 10b). The model underestimated $\beta_{gm}$ in all layers. It is noted overestimation of lidar signals at cloud bottom found in the time-height plot was not seen in the comparison of mean lidar backscattering coefficient. This could be explained as follows: the occurrence of water clouds were rather rare compared with the observations and strong attenuation was rather frequent when water clouds existed in the model. Therefore the number of grid box, where the lidar signals was well below the threshold, was large compared with that for observations. The cloud simulated top height below 3 km was often below 0.6 km and we excluded these clouds below 0.6 km when we compared them with the observations. Consequently, the simulated mean $\beta_{gm}$ became smaller.

#### 5.5.3. Frequency Distribution of Observables

[56] The comparisons of frequency distribution of the two observables were also examined for the same three height categories as in cloud fraction. We used eight bins for $dBZ_{e,gm}$ between $-55$ and 15 dBZe and ten bins were used for $\beta_{gm}$ in logarithmic scale between $-7$ and $-2.5$. In both comparisons, the grid box with cloud fraction of 0 was excluded in the estimation of frequency distribution of the observables.

[57] The models slightly overpredicted frequency of radar reflectivity with low reflectivity at $-55$ $dBZ_e$ for low-level clouds between 0.6 and 3 km. It overpredicted the fraction for reflectivity between $-35$ and $-15$ $dBZ_e$. While, the fractions of clouds with the larger reflectivity than $-10$ dBZe are much smaller than the observed ones (Figure 11a). Together with the findings in the comparisons of low-level cloud fraction, i.e., smaller frequency of large cloud fraction and small fraction of large reflectivity in the model, it was suggested that the underestimation of the fraction of large radar reflectivity in the model seemed to be related to clouds accompanying drizzle and precipitation that were not modeled. In addition, the comparisons for the frequency distribution of $\beta_{gm}$ in low-level cloud showed the model significantly under-predicted the fraction for $\beta_{gm} > 10^{-6}$ [1/m/ster] (Figure 12a). Despite of the efforts to exclude drizzle and precipitation below cloud bottom from the observed signals by using radar/lidar signals, there still remained some fraction of clouds with drizzle and precipitation in the observed data since the lidar signals due to these clouds were strongly enough to be recognized as clouds. These drizzle amount might be important in the proper estimation of radiation.

[58] The comparison of frequency distribution of radar reflectivity factor in the midlevel clouds showed that the results between the two models were quite different. R40 model showed maximum frequency at around $-25$ $dBZ_e$ and very small fraction above $-5$ $dBZ_e$, while HJI2001 model showed broader distribution of reflectivity and has its maximum frequency around $-15$ $dBZ_e$ (Figure 11b). The observed one showed its maximum at $-5$ $dBZ_e$ and smaller frequencies at lower reflectivity compared with the two models. These results indicated that the size of particles was under-predicted in the model. For lidar backscattering in midlevel clouds, R40 model overpredicted frequency for very small $\beta_{gm} < 10^{-7}$ [1/m/ster], under-predicted frequency for $10^{-7} < \beta_{gm} < 10^{-5}$ [1/m/ster] and overestimated the frequency for $\beta_{gm} > 10^{-5}$[1/m/ster] (Figure 12b).

[59] In the high-level cloud, there were differences between the models. HJI2001 model gave the larger frequency for $>-10$ $dBZ_e$ compared with R40 model. The larger frequency for $<-45$ $dBZ_e$ in the observation was found compared with the models. The peak value of frequency was found at around $-20$ $dBZ_e$ in the observations and the values were $-15$ $dBZ_e$ for R40 and around $-10$ $dBZ_e$ for HJI2001 models, respectively (Figure 11c). These showed the models tended to overpredict $r_{eff}$ in the height category. The R40 model showed overprediction of frequencies of small ($<10^{-7}$) and large ($>10^{-5}$) $\beta_{gm}$ and failed to reproduce the observed peak of the frequency at around $\beta_{gm} = 10^{-6.3}$ [1/m/ster] (Figure 12c).

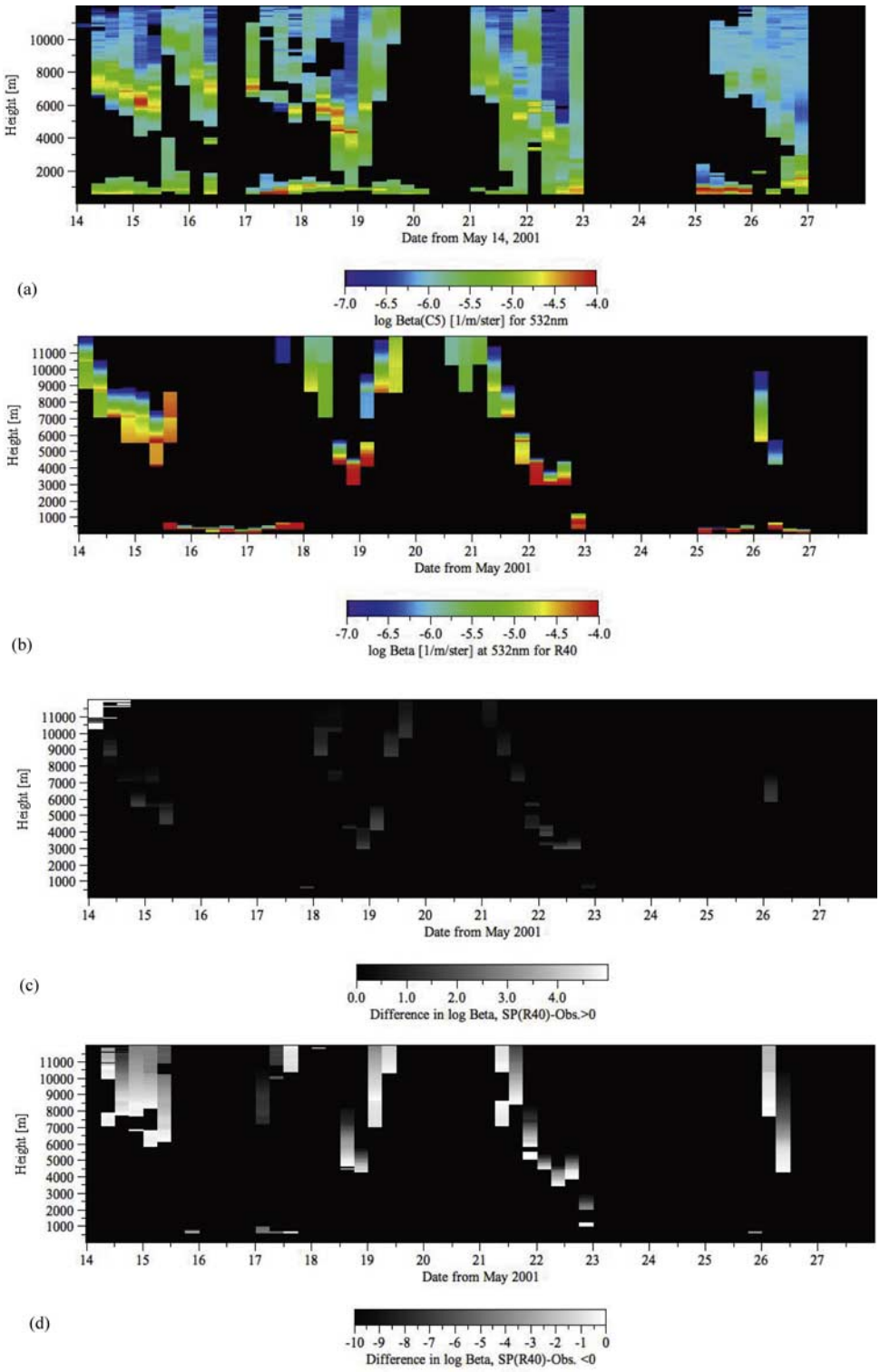


**Figure 9.** (a) Height-time cross section of the grid mean lidar backscattering coefficient $\beta$ due to cloud at 532 nm averaged over 6 hours for the observations. The cloud mask scheme C5 is applied. (b) Same as Figure 9a, for the SPRINTARS with R40 model. (c) Difference in lidar backscattering coefficient due to cloud between the SPRINTARS and the observation. Only the positive value of the difference is shown. (d) The same as Figure 9d but for negative value.

#### 5.5.4. Information Content of Combining Radar and Lidar Signals

[60] When simulated signals differ from observations, other discrepancies can arise, such as cloud position, cloud fraction, particle size, and LWC/IWC. When cloud position is accurately predicted, the combined use of radar and lidar signals may help reveal problems in predicting/assuming cloud radii and $LWC_{gm}/IWC_{gm}$ in the model. When the

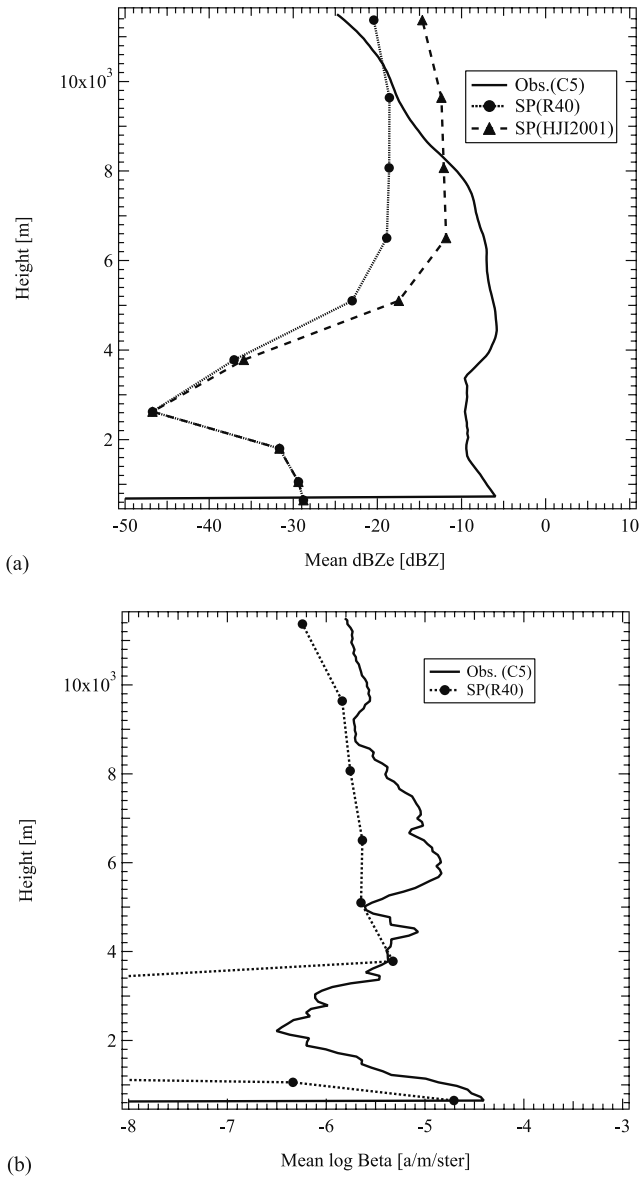


**Figure 10.** (a) Comparison between averaged vertical profiles of mean dBZe from the observation and from the models. (b) The same as Figure 10a but for $\beta$.

simulated mean cloud fraction is the same as the observed one, the question whether the predicted effective radius and $LWC_{in}/IWC_{in}$ are larger or smaller than observed can be answered. For constant IWC, radar and lidar signals are roughly proportional to $(R_{eff})^3$ and $(R_{eff})^{-1}$, respectively. If the effective radius is constant, then radar and lidar signals are proportional to LWC/IWC. From comparisons between simulations and observations, the grid box was categorized into one of the four classes, i.e., (1) simulated radar and lidar signals were both larger than the observations, (2) simulated radar and lidar signals were larger and smaller, (3) simulated radar and lidar signals were smaller and larger, and (4) both simulated radar and lidar signals were smaller. Then the following information content for cloud microphysics could be inferred from comparisons between simulations and observations. Here we have restricted our discussion to ice clouds for simplicity, but similar argu-

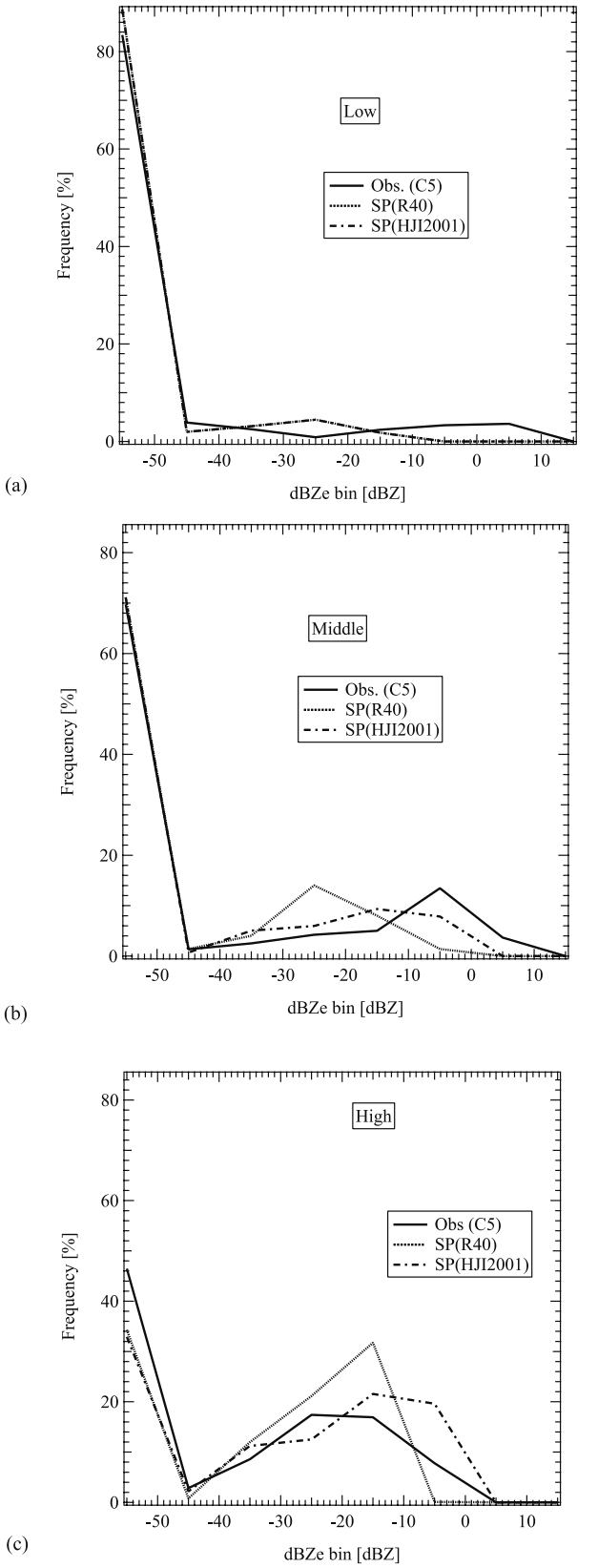


**Figure 11.** (a) Comparison of frequency distribution of dBZe from the observations and two SPRINTARS. (a) Low cloud, (b) middle cloud, and (c) high clouds.

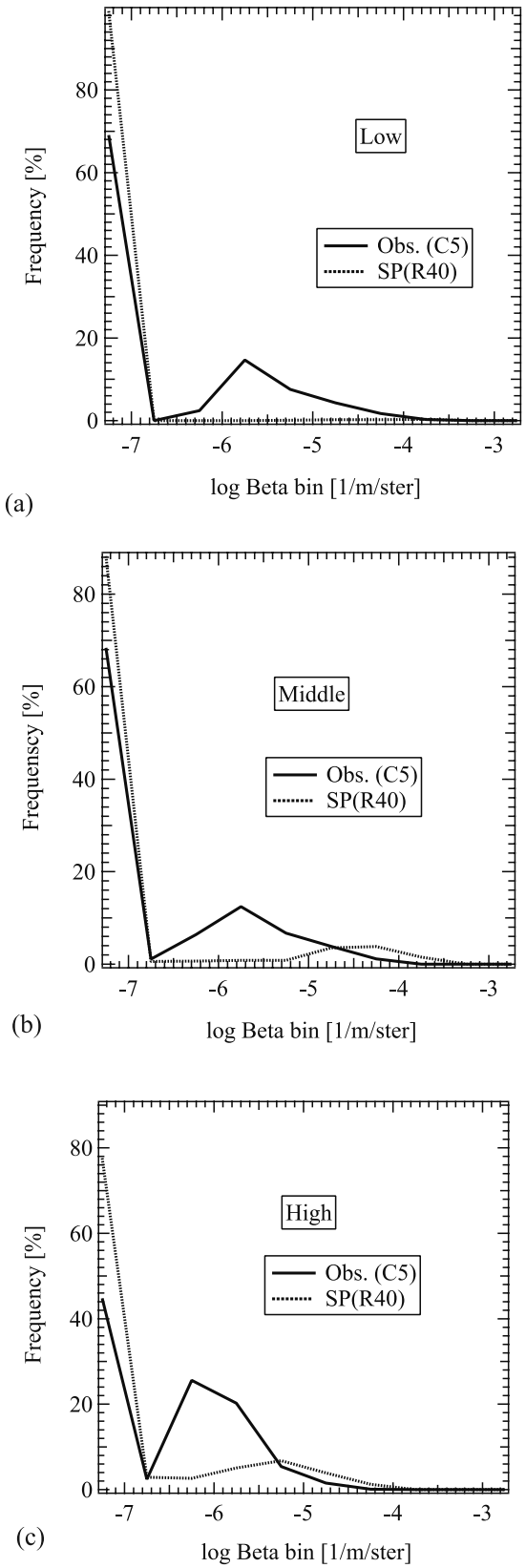


**Figure 12.** Comparison of frequency distribution of $\beta$ from the observations and the SPRINTARS with R40 model. (a) Low cloud, (b) middle cloud, and (c) high clouds.

**Table 2.** Classification of Type for Radar/Lidar Signals Between the Model and Observation

| | $\beta$ (SP) > $\beta$ (Observation) | $\beta$ (SP) < $\beta$ (Observation) |
|---|---|---|
| $dBZ_e$(SP) > $dBZ_e$ (observation) | 1: Blue | 2: Green |
| $dBZ_e$ (SP) < $dBZ_e$ (observation) | 3: Yellow | 4: Red |

ments could be applied to water clouds. The relations between observed and model signals and microphysics were also summarized in Tables 2 and 3.

[61] (1) When simulated radar and lidar signals are both larger than the observations, the property of the simulated $IWC_{gm}$ can be inferred. Overestimation of radar signals in the model implies either simulated $R_{eff}$ are larger and/or simulated $IWC_{gm}$ is larger than true value, while overestimation of lidar signals implies either simulated $R_{eff}$ is smaller and/or simulated $IWC_{gm}$ is larger than true values. Therefore it is concluded that the simulated $IWC_{gm}$ is larger and estimated $R_{eff}$ is either larger or smaller in this case.

[62] (2) When simulated radar and lidar signals are larger and smaller, respectively, the simulated $R_{eff}$ is larger than true value and we may not infer the property of $IWC_{gm}$ by the similar analyses as in 1.

[63] (3) When simulated radar and lidar signals are smaller and larger, respectively, simulated $R_{eff}$ is smaller than true value.

[64] (4) When both simulated radar and lidar signals are smaller, simulated $IWC_{gm}$ is concluded to be smaller than true value.

[65] Thus, comparisons of simulated radar and lidar signals with observed signals reveal the validity of simulated microphysics. When there are no water clouds below and the optical thickness of the clouds is relatively small, results of the discussion above can be applied to high clouds. We compared the simulated radar and lidar signals with the observations (Figures 8a, 8b, and 8e for radar signals and Figures 9a and 9b for lidar ones). The analyses for microphysics were performed only for the grid boxes where the clouds were found both in observations and simulations. The results were shown in Figure 13a for R40 model and Figure 13b for HJI2001 model, respectively. The results for the two models turned out to be similar as expected from the resemblance in the simulated radar signals between the models except for some part in high clouds.

[66] For clouds between 0.6 and 3 km, it was rare to model water clouds at the correct time and altitude as already discussed in previous sections. Simulated water clouds tend to be lower than observed, the dominant type is 2 (green), which indicates simulated radar and lidar signals were larger and smaller than observations. The simulated $R_{eff}$ of water clouds, which was around 10 $\mu$m, is generally overestimated on around 16, 17, and 25 May.

**Table 3.** Relation Between the Classification of Type Based on the Comparison of Radar/Lidar Signals and Cloud Microphysics[a]

| 1: Blue | 2: Green | 3: Yellow | 4: Red |
|---|---|---|---|
| $IWC_{gm}$(SP)+ | $R_{eff}$(SP)+ | $R_{eff}$ (SP)− | $IWC_{gm}$ (SP)− |

[a]The symbols + and − denote the overestimation and underestimation of the microphysics, for example, type "1 (blue)" means that the model IWC for grid mean value is overestimated compared with the observation.

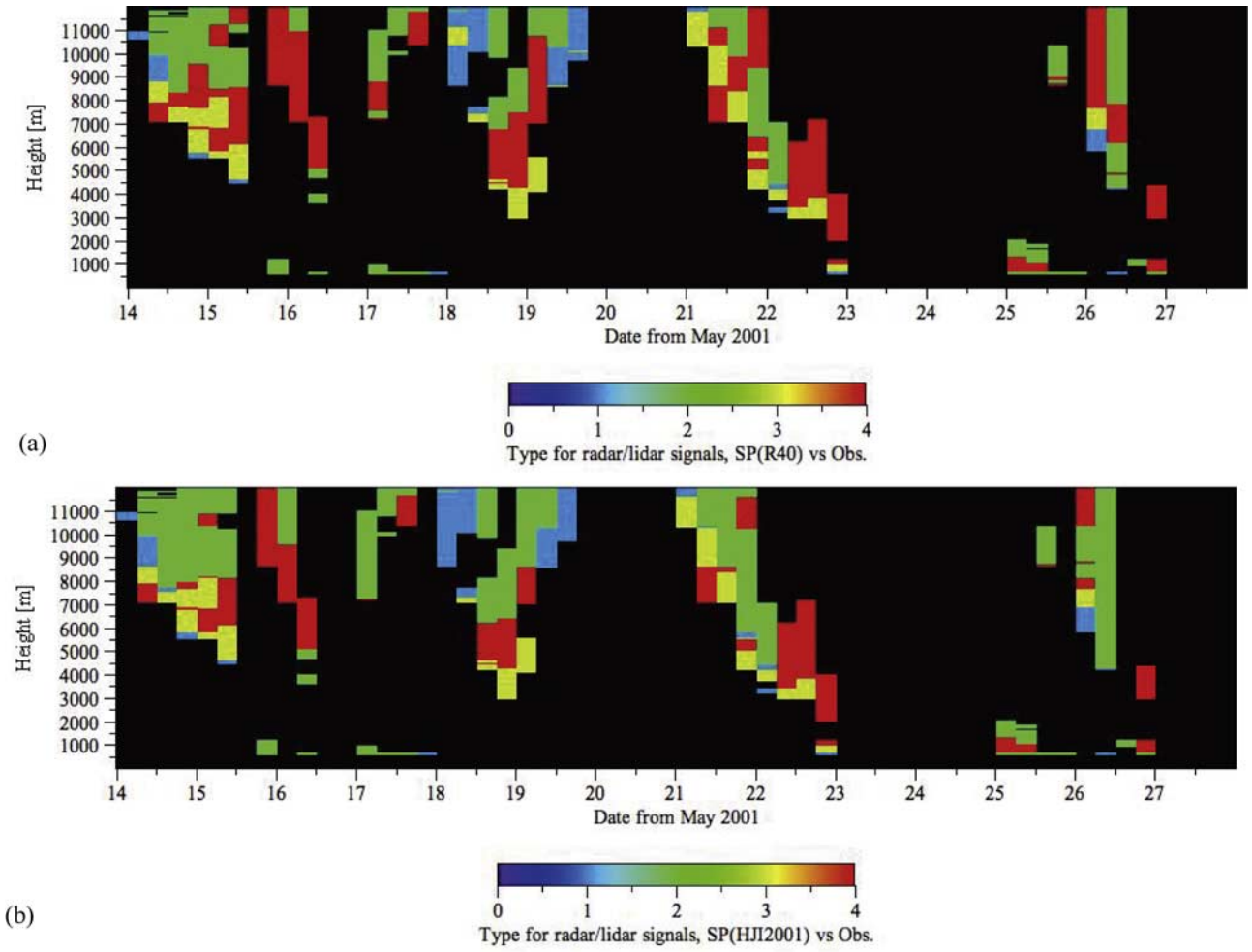


**Figure 13.** (a) Height-time cross section of type for cloud microphysics based on the comparison of radar reflectivity factor and the lidar backscattering coefficient from observation with C5 scheme and that from SPRINTARS with R40. (b) The same as Figure 13a but for HJI2001 model. The classification of type is performed when the model and observation produce the cloud in the same grid box. The number (color) is given in Table 2 and the relation between the microphysics and type is given in Table 3.

[67] For middle level between 3 and 7 km, the major type in lower part of clouds was 3 (yellow). That is, simulated radar and lidar signals were smaller and larger than observations, respectively and suggested simulated $R_{\mathrm{eff}}$ is smaller than true value, for example, from 12UTC on 14 to 12UTC on 15, from 12UTC on 18 to 12UTC on 19, and on 22 May. In the middle part of clouds in this height category, type 4 (red) was dominant, indicating the simulated ice and water content were smaller than true values.

[68] For clouds above 7 km, only ice clouds existed in these grids in the model. In both models of R40 and HJI2001, the dominant type was 2; that is, the simulated $R_{\mathrm{eff}}$ of 40 $\mu$m was larger than the true value of $R_{\mathrm{eff}}$. There was a difference in the results between R40 and HJI2001 models in this height category. In the HJI2001 model, the dominant type was 2 while type 4 was minor and was comparable to type 1 (blue). In the R40 model, fraction of type 4 was larger compared with HJI2001 model, though type 2 was still the major one. In both models, type 1 occurred at the same position and time at 0-12UTC on 18 and 12-24UTC on 19 May, where $\mathrm{IWC}_{\mathrm{gm}}$ was overestimated in the models at the outer part of the clouds. Further analysis may be possible using algorithms such as the radar/lidar algorithm; future results using the same data will be reported.

[69] Aerosols can be studied by comparing simulated and observed lidar signals. A dense aerosol layer was observed by lidar below 1 km. This layer was reproduced in the simulation as well. An aerosol plume was present between 20 and 21 May. SPRINTARS analysis verified that the aerosols were dust that originated in the Gobi Desert. Further study of the nature of the aerosols observed during the cruise is beyond the scope of this paper. *Nishizawa et al.* [2006] presented a detailed discussion of microphysics of aerosols in the same cruise data and the validity of SPRINTARS in terms of aerosols.

## 6. Summary

[70] Clouds and aerosols were observed over the Pacific Ocean near Japan in May 2001 by a shipborne 95-GHz

cloud radar and a lidar on the Research Vessel Mirai. We applied five cloud mask schemes to yield cloud and drizzle occurrence from the radar and lidar signals. Then these observed radar and lidar signals due to clouds were used to validate the representation of cloud occurrence and its microphysics in the General Circulation Model.

[71] Among the five cloud mask schemes, the scheme C4 relies on radar or lidar signals to determine hydrometeor occurrence and scheme C5 is similar to C4 but uses lidar for water cloud base and is considered to be the reference scheme to retrieve clouds. The difference between C4 and C5 corresponds to drizzle occurrence and the frequency of occurrence turned out to be about half of the frequency of occurrence of clouds (20%) at 1 km.

[72] The vertical distribution of the mean cloud frequency showed local minimum below 2 km occurred at 1 km; the mean cloud occurrence was about 20% and local maxima at 7.4 and 10.5 km, with mean cloud occurrences of 40% and 35%, respectively. These two maxima correspond to the amount of relative humidity. For the other measurements from active sensors over land in midlatitude, we considered the following two studies. *Mace et al.* [1998a, 1998b] examined the vertical frequency of hydrometeor occurrence during winter season 1996/1997 from mm-cloud radar at ARM SGP sire in Oklahoma, USA and showed that local maximum of frequency are about 25% below 2 km and also about 35% at 7 km. The minimum is located at around 3 km and the value is 16%. It is noted that the frequency of occurrence in their study, by definition, corresponds to the maximum of mean cloud fraction in this study. The analysis of the mm-radar at Chilbolton in England [*Hogan et al.*, 2001] shows that maximum of mean cloud fraction are 25% at 1.6 km and 22% at 5.5 km and minimum is found at 4 km and the value is 17%. The general vertical structures between the three data sources agree except for the locations of local maximum and minimum as well as the additional local maximum above 8 km found in the Mirai data. That is, the local maximum of mean cloud fraction above 4 km in the Mirai data is larger than those in ARM SGP and Chilbolton data and there is no local maximum at 10 km in data in the both sites over land contrary to the Mirai data. The value of local minimum between 2 and 4 km in the Mirai data is smaller than other two results. It is concluded that there is larger contrast between the upper cloud fraction and lower/midlevel ones in the Mirai data than the other two data over land.

[73] Multilayer structures of clouds were investigated using C5. Probabilities of zero, one, two, three, and four or more layers were 20, 48, 23, 7, and 2%, respectively, during the cruise. The average number of layers when clouds existed was 1.54. These values are close to the finding by *Wang et al.* [2000] from the 20-year radio-sonde data.

[74] The cloud fraction derived from radar and lidar observations was used to test the SPRINTARS model, which is based on the NIES-CCSR GCM with nudging by NCEP-NCAR reanalysis data. In order to take into account the sensitivity of instruments, simulated radar and lidar signals in cloud should be estimated prior to the comparisons between observations and the models. Then simulated cloud fraction was derived by the application of the cloud mask scheme to the simulated signals by SPRINTARS. The model patterns resembled the observations. However, the model overestimated clouds above 8 km by about 60% and underestimated them below 8 km. The tendency to overestimate cloud fraction increased as the altitude increased. The model failed to predict some fraction of the water clouds around 1 km that were detected by the observations and underestimated height of water clouds.

[75] Comparison of radar reflectivity and lidar backscattering coefficient between observations and the model was performed. The model $dBZ_e$ near the cloud bottom was smaller than observed. Above 10 km, the model overestimated $dBZ_e$ compared with the observation. Simulated lidar signal was strongly attenuated whereas actual observations were not. Model extinction was overestimated in water cloud bottom in the model.

[76] Frequency distribution of cloud fraction, radar reflectivity factor, and lidar backscattering coefficient in grid mean were examined and compared between the observations and the models in three height categories. In the all three categories, the model failed to predict the frequency distribution of cloud fraction and the two observables.

[77] Finally we investigated the information content from the comparison of radar and lidar signals between the observation and the model simulations. This method was used instead of a direct comparison of cloud microphysics by retrieval algorithms. It was shown that the comparisons of signals were effective to validate model cloud microphysics. Simulated particle sizes in water clouds of about 10 $\mu$m were larger than observed. At upper levels, the ice particle size in the model was larger than the observed value. Radar and lidar observation data will be available from two satellites that were launched in 28 April 2006 as part of the NASA Earth System Science Pathfinder (ESSP) program. CloudSAT carries a 95-GHz radar [*Stephens*, 2002]. Cloud-Aerosol Lidar and Infrared Pathfinder Satellite Observations [CALIPSO; *Winker et al.*, 2002] includes lidar at 0.532 and 1.064 $\mu$m. European and Japanese satellite mission, EarthCARE, will follow CloudSAT and CALIPSO experiments. It is therefore vital to understand the information latent in combining 95-GHz radar and lidar systems over wide area as shown here.

[78] **Acknowledgments.** We thank Dr. Yoneyama at JAMSTEC for conducting the atmospheric observation mission on the Research Vessel Mirai and also providing us the data of sky camera, radio sonde, and rain gauge. We thank Dr. Iwasaki at the National Defense Academy of Japan for the discussions on calibration of cloud radar. This work was partly supported by the Ministry of Education, Culture, Sports, Science, and Technology through a Grant-in-Aid for Scientific Research (14702014) and (19340132) and a Grant-in-Aid for JSPS Fellows (16·2254), by Core Research for Evolutional Science and Technology (CREST) of the Japan Science and Technology Agency, and by the Global Environment Research Fund by Ministry of Environment Japan B-4.

## References

Arakawa, A., and W. H. Schubert (1974), Interaction of a cumulus cloud ensemble with the large-scale environment. Part I, *J. Atmos. Sci.*, *31*, 674–701.

Astin, I., L. D. Girolamo, and H. M. van de Poll (2001), Baysian confidence intervals for true fractional coverage from finite transect measurements: Implications for cloud studies from space, *J. Geophys. Res.*, *106*, 17,303–17,310.

Chang, F.-L., and Z. Li (2005), A new method for detection of cirrus overlapping water clouds and determination of their optical properties, *J. Atmos. Sci.*, *62*(11), 3993–4009.

Clothiaux, E. E., T. P. Ackerman, G. G. Mace, K. P. Moran, R. T. Marchand, M. A. Miller, and B. E. Martner (2000), Objective determi-

nation of cloud heights and radar reflectivities using a combination of active sensors at the ARM CART sites, *J. Appl. Meteorol.*, *39*, 645–665.
Donovan, D. P., and A. C. A. P. van Lammeren (2001), Cloud effective particle size and water content profile retrievals using combined lidar and radar observations: Part I. Theory and simulations, *J. Geophys. Res.*, *106*, 27,425–27,448.
Ghan, S. J., L. R. Leung, R. C. Easter, and A. Abdul-Razzak (1997), Prediction of cloud droplet number in a general circulation model, *J. Geophys. Res.*, *102*, 21,777–21,794.
Heymsfield, A. (1986), Notes and correspondence: Ice particles observed in a cirriform cloud at -83 °C and implications for polar stratospheric clouds, *J. Atmos. Sci.*, *43*, 851–855.
Hogan, R. J., and A. J. Illingworth (2000), Deriving cloud overlap statistics from radar, *Q.J.R. Meteorol. Soc.*, *126*, 2903–2909.
Hogan, R. J., C. Jakob, and A. J. Illingworth (2001), Comparison of ECMWF winter-season cloud fraction with radar derived values, *J. Appl. Meteorol.*, *40*(3), 513–525.
Hogan, R. J., M. D. Behera, E. J. O'Connor, and A. J. Illingworth (2004), Estimate of the global distribution of stratiform supercooled liquid water clouds using the LITE lidar, *Geophys. Res. Lett.*, *31*, L05106, doi:10.1029/2003GL018977.
Horie, H., T. Iguchi, H. Hanado, H. Kuroiwa, H. Okamoto, and H. Kumagai (2000), Development of a 95-GHz airborne cloud profiling radar (SPIDER): Technical aspects, *IEICE Trans. Commun.*, *E83-B(No. 9)*, 2010–2020.
Ishimoto, H., and K. Masuda (2002), A Monte Carlo approach for the calculation of polarized light: Application to an incident narrow beam, *J. Quant. Spectrosc. Radiat. Transfer*, *72*, 467–483.
Iwasaki, S., et al. (2004), Subvisual cirrus cloud observations using a 1064-nm lidar, a 95-GHz cloud radar, and radiosondes in the warm pool region, *Geophys. Res. Lett.*, *31*, L09103, doi:10.1029/2003GL019377.
Le Treut, H., and Z.-X. Li (1991), Sensitivity of an atmospheric general circulation model to prescribed SST changes: Feedback effects associated with the simulation of cloud optical properties, *Clim. Dyn.*, *5*, 175–187.
Mace, G. G., T. P. Ackerman, and E. E. Clothiaux (1997), A study of composite cirrus morphology using data from a 94-GHz radar and correlations with temperature and large-scale vertical motion, *J. Geophys. Res.*, *102*, 13,581–13,593.
Mace, G. G., C. Jakob, and K. P. Moran (1998a), Validation of hydrometeor occurrence predicted by the ECMWF model using millimeter wave radar data, *Geophys. Res. Lett.*, *25*, 1645–1648.
Mace, G. G., K. Sassen, S. Kinne, and T. P. Ackerman (1998b), An examination of cirrus cloud characteristics using data from millimeter wave radar and lidar: The 24 April SUCCESS case study, *Geophys. Res. Lett.*, *25*, 1133–1136.
Mace, G. G., E. E. Clothiaux, and T. P. Ackerman (2001), The composite characteristic of cirrus clouds: Bulk properties revealed by one year of continuous cloud radar data, *J. Clim.*, *14*, 2185–2203.
Matrosov, S. Y., B. W. Orr, R. A. Kropfli, and J. B. Snider (1994), Retrieval of vertical profiles of cirrus cloud microphysical parameters from Doppler radar and infrared radiometer measurements, *J. Appl. Meteorol.*, *33*, 617–626.
Matrosov, S. Y., T. Uttal, and D. A. Hazen (2004), Evaluation of radar reflectivity-based estimates of water content in stratiform marine clouds, *J. Appl. Meteorol.*, *43*, 405–419.
McClatchey, R. A., R. W. Fenn, J. E. A. Selby, F. E. Volz, and J. S. Garing (1972), Optical properties of the atmosphere, 3rd ed, *AFCRL Environ. Res. Papers*, *AFCRL-72-0497*, 108 pp.
Moorthi, S., and M. J. Suarez (1992), Relaxed Arakawa-Schubert: A parameterization of moist convection for general circulation models, *Mon. Weather Rev.*, *120*, 978–1002.
Nishizawa, T., H. Okamoto, N. Sugimoto, I. Matsui, A. Shimizu, and K. Aoki (2007), An algorithm that retrieves aerosol properties from dual-wavelength polarized lidar measurements, *J. Geophys. Res.*, *112*, D06212, doi:10.1029/2006JD007435.
Okamoto, H. (2002), Information content of the 95-Ghz cloud radar signals: Theoretical assessment of effects of nonsphericity and error evaluation of the discrete dipole approximation, *J. Geophys. Res.*, *107*(D22), 4628, doi:10.1029/2001JD001386.
Okamoto, H., S. Iwasaki, M. Yasui, H. Horie, H. Kuroiwa, and H. Kumagai (2000), 95-GHz cloud radar and lidar systems: Preliminary results of cloud microphysics, *Proc. SPIE*, *4152*, 355–363.
Okamoto, H., S. Iwasaki, M. Yasui, H. Horie, H. Kuroiwa, and H. Kumagai (2003), An algorithm for retrieval of cloud microphysics using 95-GHz cloud radar and lidar, *J. Geophys. Res.*, *108*(D7), 4226, doi:10.1029/2001JD001225.
Platt, C. M. R. (1973), Lidar and radiometric observations of cirrus clouds, *J. Atmos. Sci.*, *30*, 1191–1204.
Rogers, R. R., and M. K. Yau (1989), A short course in cloud physics, 3rd ed, 290 pp. Elsevier, New York.
Rossow, W. B., and R. A. Schiffer (1999), Advances in understanding clouds from ISCCP, *Bull. Am. Meteorol. Soc.*, *80*, 2261–2287.
Rossow, W. B., Y. Zhang, and J. Wang (2005), A statistical model of cloud vertical structure based on reconciling cloud layer amounts inferred from satellites and radiosonde humidity profiles, *J. Clim.*, *18*, 3587–3605.
Stephens, G. L. (2002), The CloudSat mission and the A-train. A new dimension of space-based observations of clouds and precipitation, *Bull. Am. Meteorol. Soc.*, *83*, 1771–1790.
Sugimoto, N., I. Matsui, Z. Liu, A. Shimizu, and K. Asai (2001), Latitudinal distribution of aerosols and clouds in the western Pacific observed with a lidar on board the research vessel Mirai, *Geophys. Res. Lett.*, *28*, 4187–4190.
Sugimoto, N., I. Matsui, A. Shimizu, I. Uno, K. Asai, T. Endoh, and T. Nakajima (2002), Observation of dust and anthropogenic aerosol plumes in the Northwest Pacific with a two-wavelength polarization lidar on board the research vessel Mirai, *Geophys. Res. Lett.*, *29*(19), 1901, doi:10.1029/2002GL015112.
Takemura, T., H. Okamoto, Y. Maruyama, A. Numaguti, A. Higurashi, and T. Nakajima (2000), Global three-dimensional simulation of aerosol optical thickness distribution of various origins, *J. Geophys. Res.*, *105*, 17,853–17,873.
Takemura, T., T. Nozawa, S. Emori, T. Y. Nakajima, and T. Nakajima (2005), Simulation of climate response to aerosol direct and indirect effects with aerosol transport-radiation model, *J. Geophys. Res.*, *112*, D02202, doi:10.1029/2004JD005029.
Wang, Z., and K. Sassen (2002), Cirrus cloud microphysical property retrieval using lidar and radar measurements: Part I. Algorithm description and comparison with in situ data, *J. Appl. Meteorol.*, *41*, 218–229.
Wang, J., W. Rossow, and Y. Zhang (2000), Cloud vertical structure and its variations from a 20-Yr global rawinsonde dataset, *J. Clim.*, *13*, 3041–3056.
Winker, D. M., J. Pelon, and M. P. McCormick (2002), The CALIPSO mission: Spaceborne lidar for observation of aerosols and clouds, *Proc. SPIE*, *4893*, 1–11.

S. Emori, I. Matsui, A. Shimizu, and N. Sugimoto, National Institute for Environmental Studies, Tsukuba, Ibaraki 305-8505, Japan. (i-matsui@nies.go.jp; nsugimot@nies.go.jp)
A. Kamei, National Institute of Advanced Industrial Science and Technology, Tsukuba 305-8568, Japan. (a.kamei@aist.go.jp)
H. Kumagai and H. Kuroiwa, National Institute of Information and Communications Technology, Koganei, Tokyo 184-8795, Japan. (kumagai@nict.go.jp; kuroiwa@nict.go.jp)
T. Nakajima, Center for Climate System Research, The University of Tokyo, 5-1-5 Kashiwanoha, Kashiwa, Chiba 277-8568, Japan. (teruyuki@ccsr.u-tokyo.ac.jp)
T. Nishizawa, Meteorological Research Institute, Nagamine 1-1, Tsukuba, Ibaraki 305-0052, Japan. (nisizawa@mri-jma.go.jp)
H. Okamoto, Center for Atmospheric and Oceanic Studies, Graduate School of Science, Tohoku University, Sendai 980-8578, Japan. (okamoto@caos-a.geophys.tohoku.ac.jp)
T. Takemura, Research Institute for Applied Mechanics, Kyushu University, Kasuga, Fukuoka 816-8580, Japan. (toshi@riam.kyushu-u.ac.jp)